Electronic Supplementary Material (ESI) for Journal of Materials Chemistry A.

Supporting Information (SI) for:

Stabilizing Oxygen Intermediates on Redox-Flexible Active Sites in Multimetallic Ni-Fe-Al-Co Layered Double Hydroxide Anodes for Excellent Alkaline and Seawater Electrolysis

Enkhbayar Enkhtuvshin[a,†], *Kang Min Kim*[b,†], *Young-Kwang Kim*[c,†], *Sungwook Mihn*[d], *So Jung Kim*[a], *Sun Young Jung*[a], *Nguyen Thi Thu Thao*[a], *Ghulam Ali*[e], *Muhammad Akbar*[f], *Kyung Yoon Chung*[f,g], *Keun Hwa Chae*[h], *Sukhyun Kang*[b], *Taeg Woo Lee,*[b] *Hyung Giun Kim,*[b] *Seunggun Choi*[i] *and HyukSu Han*[a,*]

a. Department of Energy Engineering, Konkuk University, 120 Neungdong-ro, Gwangjin-gu, Seoul 05029, Republic of Korea

b. Korea Institute of Industrial Technology, 137-41 Gwahakdanji-ro, Gangneung-si, Gangwon 25440, Republic of Korea

c. Technical Laboratory, Vitual Lab Inc., 49 Achasan-ro, Seoul, 04799, Republic of Korea

d. Department of Advanced Materials Engineering, Kyonggi University, Suwon 16227, Republic of Korea

e. U.S.-Pakistan Center for Advanced Studies in Energy (USPCASE), National University of Sciences and Technology (NUST), H-12, Islamabad, Pakistan

f. Center for Energy Storage Research, Korea Institute of Science and Technology, Hwarang-ro 14-gil 5, Seongbuk-gu, Seoul 02792, Republic of Korea

g. Division of Energy and Environment Technology, KIST School, Korea University of Science and Technology, Seoul 02792, Republic of Korea

h. Advanced Analysis Center, Korea Institute of Science and Technology, Seoul 02792, Republic of Korea

i. Department of Energy Engineering, Hanyang University, 222 Wangsimni-ro, Seoul 133-791, Republic of Korea

Chemicals: All chemicals were purchased from Sigma Aldrich and used without further purifications (United States, ACS reagents grades). Carbon cloth (CC) was purchased from WizMAC Inc. (Republic of Korea, thickness: 0.6 mm, specific surface area: 800 m^2/g).

Preparation of CC support: CC was cleaned in the mixture of nitric acid and DI water solution with a volume ratio 3:1 for 1 h at 100°C. The solution was stirred at 100 rpm during 1 h. Then, subsequent washing was followed using water and ethanol for several times. The cleaned CC was dried at room temperature overnight.

Synthesis of Ni-LDHs: Typically, as-prepared CC was immersed in 100 ml of DI water. 1.141 g of Ni (II) chloride hexahydrate ($NiCl_2 \cdot 6H_2O$) was dissolved in the solution at room temperature, and then sonication was performed about 10 min in order to perfectly dissolve Ni precursor. The resulting mixture was transferred to a 120-mL Teflon®-lined stainless-steel autoclave and hydrothermally reacted at 120°C for 3 h. The resultant product was washed several times using DI water and ethanol. Subsequently, the final product was dried under air at room temperature for overnight.

Synthesis of NF-LDHs: Synthesis method for NF-LDHs was same as that of Ni-LDHs, except that 0.298 g of iron (II) chloride tetrahydrate ($FeCl_2 \cdot 4H_2O$) was added to the solution before hydrothermal reaction.

Synthesis of NFA-LDHs: Synthesis method for NFA-LDHs was same as that of NF-LDHs, except that 0.15 g of aluminum tetrachloride ($AlCl_3$) was added to the solution before hydrothermal reaction.

Synthesis of NFAC-LDHs: 1.46 g of $Co(NO_3 \cdot 6H_2O)$ and 5 mg of cetrimonium bromide ($CH_3(CH_2)_{15}N(Br)(CH_3)_3$, CTAB) were dissolved in a 100 ml of methanol. In addition, 3.28 g of 2-methylimidazole was dissolved in a 100 ml of methanol by stirring about 10 min at 200 rpm. Same volume amount of each solutions were homogeneously mixed together, and then the NFA-LDHs was placed at the middle of solution for aging 24 h at room temperature. During aging process, ZIF-67 was homogeneously deposited onto the NFA-LDHs nanosheets. The resulting NFAC-LDHs was washed with DI water and ethanol for several times. Subsequently, the final product was dried under air at room temperature for over night

Synthesis of NFAC-MELDHs: NFAC-LDHs was electrochemically activated via a 50 continuous cyclic voltammetry (CV) cycles in an OER potential window (1.23 ~ 1.60 V_{RHE}) in a 1.0 M KOH solution using a scan rate of 50 mV s^{-1}. During the CV cycling, the Co atoms in ZIF-67 were incorporated into NFAC-LDHs with a homogeneous chemical blend of different metals.

Synthesis of NFAC-MELDHs via one-step hydrothermal route: 1.141 g of Ni (II) chloride hexahydrate ($NiCl_2 \cdot 6H_2O$), 0.183 g of iron (II) chloride tetrahydrate ($FeCl_2 \cdot 4H_2O$), 0.012 g of aluminum tetrachloride ($AlCl_3$), and 0.027 g of $Co(NO_3 \cdot 6H_2O)$ were dissolved in 100 ml of DI water at room temperature where the as-prepared CC was placed, and then sonication was performed for about 10 min in order to perfectly dissolve Ni precursor. The resulting mixture was transferred to a 120-mL Teflon®-lined stainless-steel autoclave and hydrothermally reacted at 120°C for 3 h. The resultant product was washed several times using DI water and ethanol. Subsequently, the final product was dried under air at room temperature for overnight.

Determination of Electrochemical Double Layer Capacitance (C_{dl}): The CV test was conducted in an O_2-saturated 1 M KOH solution to estimate the C_{dl} at non-faradaic potentials (1.1 V_{RHE} ~ 1.2 V_{RHE}). CV measurements were performed at various scan rates (20, 40, 60, 80, 100, and 120 mV s^{-1}). The difference in current density between the anodic and cathodic sweeps (J_{anodic}–$J_{cathodic}$) at the middle of potential range was plotted as a function of the scan rate, where the slope has a linear relationship with the C_{dl} of the catalyst.

$$C_{dl} = \frac{j_a - j_c}{2 \times \upsilon} = \frac{j_a + |j_c|}{2 \times \upsilon} = \frac{\Delta j}{2 \times \upsilon}$$

(1)

where j_a and j_c are the anodic and cathodic current density, respectively, recorded at the middle of the selected potential range and υ is the sweep rate.

Determination of Electrochemical Surface Area (ECSA): The ECSAs of samples have been attained from the measured C_{dl}. The current generated in the non-Faradaic region is due to charging of double layer and shows linear relationship with the active surface area. Generally, the specific capacitance of 1cm^2 flat surface area is equal to C_{dl} value of 20 – 60 μF cm^{-2} with an average value of 40 μF cm^{-2}.[3] Hence, the C_{dl} can be converted to the ECSA as below.

$$ECSA = C_{dl} \text{ of catalyst } (mF\ cm^{-2})/0.04\ (mF\ cm^{-2}) \qquad (2)$$

Density Functional Theory Calculations: Density functional theory (DFT) calculations were performed using the generalized gradient approximation (GGA) with Perdew–Burke–Ernzerhof (PBE) parameterization and quantum espresso (QE) from Materialssquare Inc. To investigate the catalytic mechanism of nickel-based LDHs more precisely, we did not use an anhydrous β-NiOOH-type phase shown in several studies[4,5] but a γ-NiOOH-type phase, in which water and cations are intercalated between layers.[6] For cell shape and volume relaxations of (oxy)hydroxide compounds, we used 2 × 2 × 4 k-point grids and a 90 Ry energy cutoff of the wave function, which ensured electronic and ionic convergence. The convergence criterions of the structural relaxation and electronic self-consistency for energy and forces set were chosen as 10^{-8} Ry and 0.000038 Ry/bohr, respectively. To evaluate the solvation energy of OER intermediates, an 20Å thick vacuum-layer was placed within the periodic cells repeated in the x-axis to obviate interactions. We also considered the van der Waals interactions using DFT-D3(BJ) method. Note that all calculations were spin-polarised.

We calculated the reaction free energy diagram of oxygen evolution:

$4OH^{-} + * \rightarrow 3OH^{-} + OH^{*} + e^{-} \rightarrow 2OH^{-} + O^{*} + H_2O + 2e^{-} \rightarrow OH^{-} + OOH^{*} + H_2O + 3e^{-} \rightarrow OO^{*} + 2H_2O + 4e^{-} \rightarrow O_2 + 2H_2O + 4e^{-} + *$.

A recent study showed that under OER conditions, the under-coordinated surface O in MFe-OOH (M: transition metals) is expected to be saturated with hydrogen to form bridge OH species. Simultaneously, under-coordinated metal sites become saturated with the atop OH species when the surface approaches equilibrium in the electrolyte. Hence, we applied a Mars van Krevelen-type mechanism to calculate the reaction free energy diagram.

In this model, the first reaction step starts from the deprotonation of surface OH taking place at the in situ surface phase rather than initiating from OH adsorption. Accordingly, the binding energies were calculated for O*, OOH*, and OO* intermediates at the most favorable adsorption sites for each LDH system. The Gibbs free energy for absorption was computed by a method proposed by Nørskov for each reaction step based on the four-electron reaction pathway in alkaline media, which can be written as follows:

$$\Delta G(O^{*}) = G(O^{*}) - G(OH^{*}) + 0.5\mu_{H_2}^{0} + \Delta G_U + \Delta G_{pH} \tag{3}$$

$$\Delta G(OOH^{*}) = G(OOH^{*}) - G(OH^{*}) + \mu_{H_2}^{0} - \mu_{H_2O}^{0} + \Delta G_U + \Delta G_{pH} \tag{4}$$

$$\Delta G(OO^*) = G(OO^*) - G(OH^*) + 1.5\mu_{H_2}^0 - \mu_{H_2O}^0 + \Delta G_U + \Delta G_{pH} \quad (5)$$

where $\Delta G(O^*)$, $\Delta G(OOH^*)$ and $\Delta G(OO^*)$ are the absorption energies for intermediates (O, OOH, OO) adsorbed on the surface, $\mu_{H_2}^0$ and $\mu_{H_2O}^0$ chemical potential of H_2(g) and H_2O(g), ΔG_U electron energy shift by bias, and ΔG_{pH} the free energy of H^+-ions. In this work, the calculation condition was set to pH = 0, thus the correction value ΔG_{pH} can be ignored. ΔG_U is -eU, where U was the potential of the electrode relative to the standard hydrogen electrode. G_i and μ_i^0 can be expressed as follows:

$$G_i = E_i + ZPE_i - TS_i \text{ and } \mu_i^0 = E_i^0 + ZPE_i - TS_i \quad (6)$$

where E_i is the energy of individual adsorbed intermediate (O, OOH, OO) obtained from DFT calculations. E_i^0 energy of H_2 and H_2O molecules obtained from DFT calculations, ZPE zero-point energy, S entropy. ZPE and S are shown in Table S1. RDS was determined as the reaction step where the highest energy barrier ($\Delta Gi - \Delta Gii$, i and ii are the initial and final reaction steps, respectively) presents. Overpotential was calculated as the potential difference between one that requires to induce down-hill energy landscapes for all reaction steps involved in OER and the equilibrium potential of 1.23 V.

Table S1. ZPE corrections (T = 298 K) and entropy contributions for gaseous molecules and reactants on LDH`s surface.

System	ZPE (eV)	TS (eV)
H_2O(g)	0.56[a]	0.67[a]
H_2(g)	0.27[a]	0.41[a]

O*	0.084[b]	0.05[b]
OH*	0.386[b]	0.07[b]
OOH*	0.457[b]	0.16[b]
OO*	0.155[c]	0.1[c]

[a] P. W. Atkins, Physical Chemistry, sixth ed., Oxford University Press, Oxford (1998).

[b] M. Li et al., Journal of Catalysis 314 (2014) 66.

[c] Mean value among O, OH and OOH

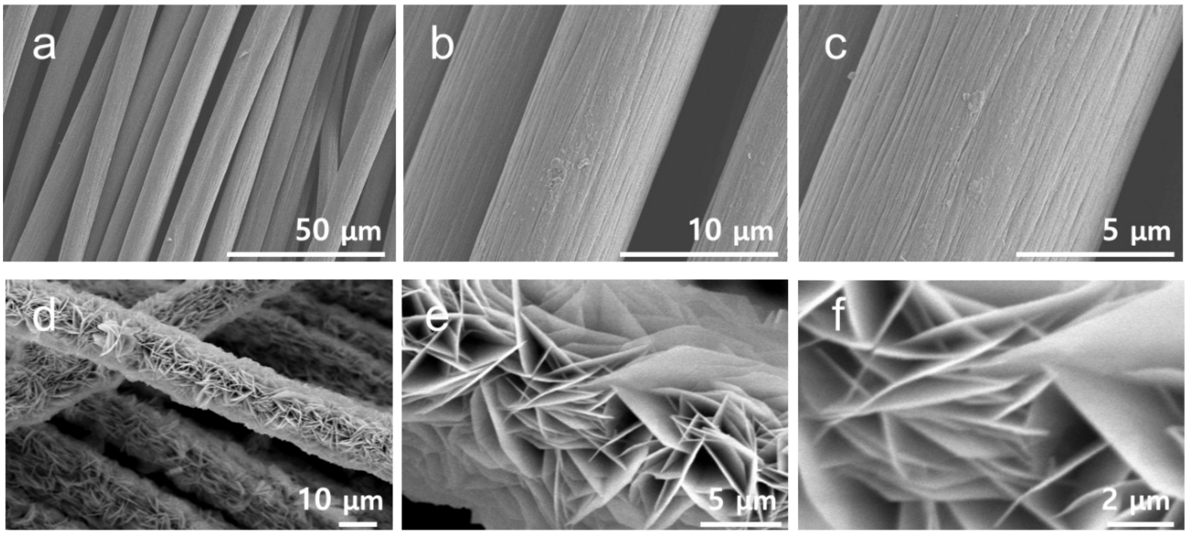

Figure S1. SEM images of (a-c) bare CC and (d-f) Ni-LDHs.

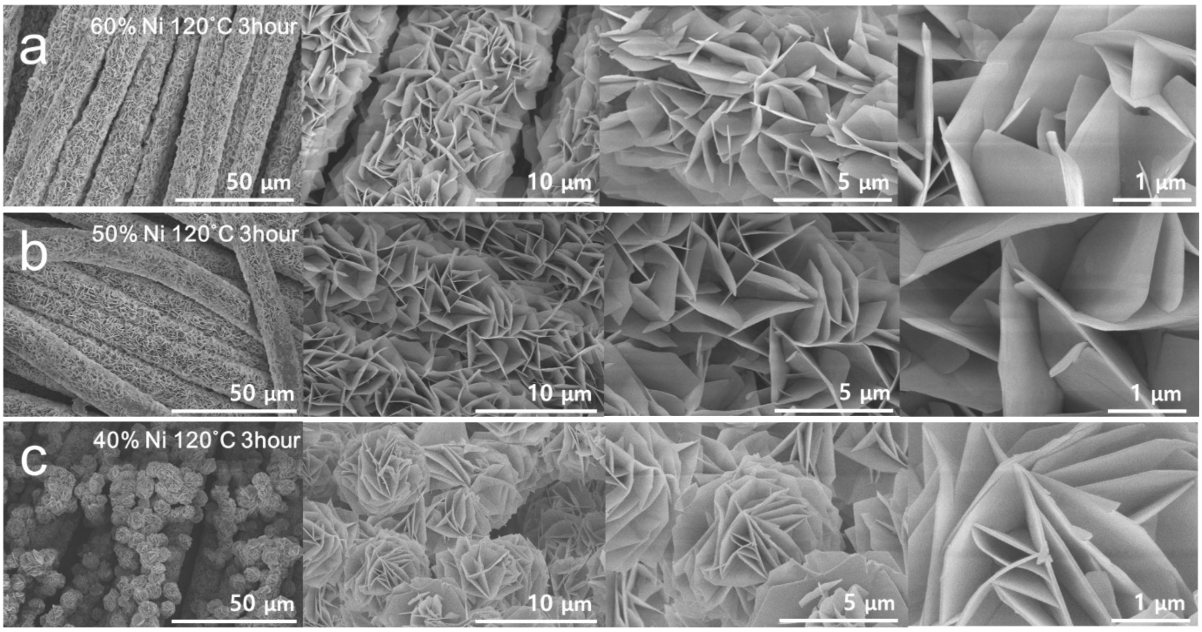

Figure S2. SEM images of Ni-LDHs with different amounts of Ni precursor. Percentage in the labels means relative mass ratio of Ni (II) chloride hexahydrate ($NiCl_2 \cdot 6H_2O$) compared to 2.282 g.

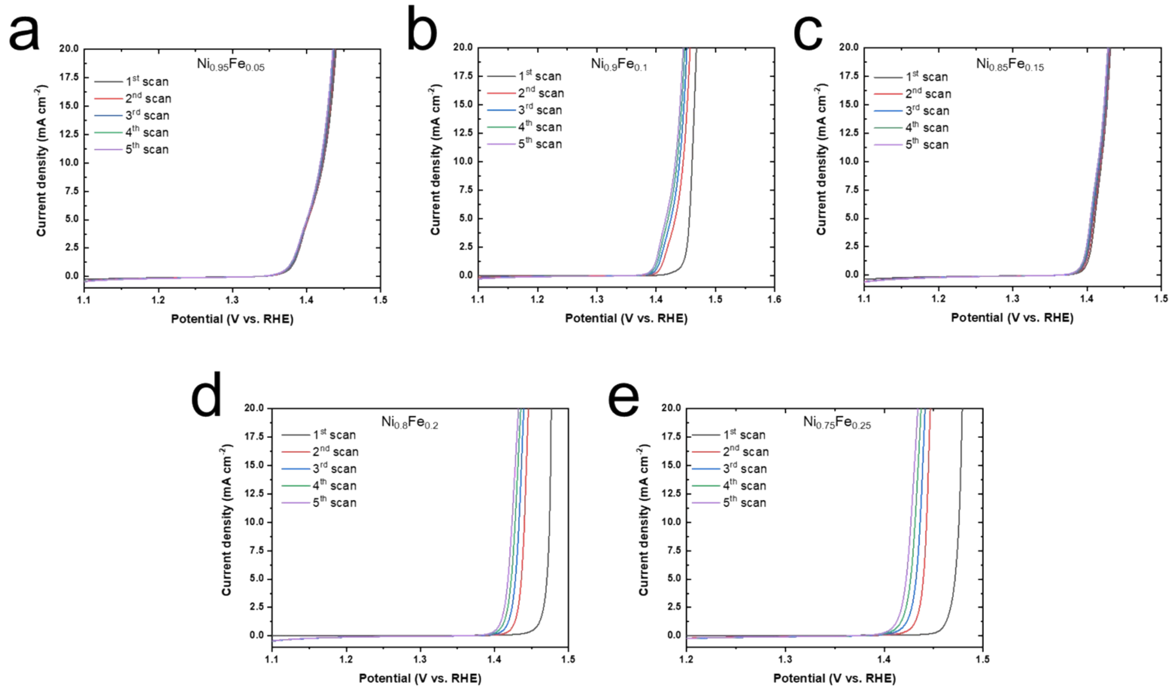

Figure S3. LSV curves for NF-LDHs with different molar ratios of Ni:Fe measured in 1.0 M KOH.

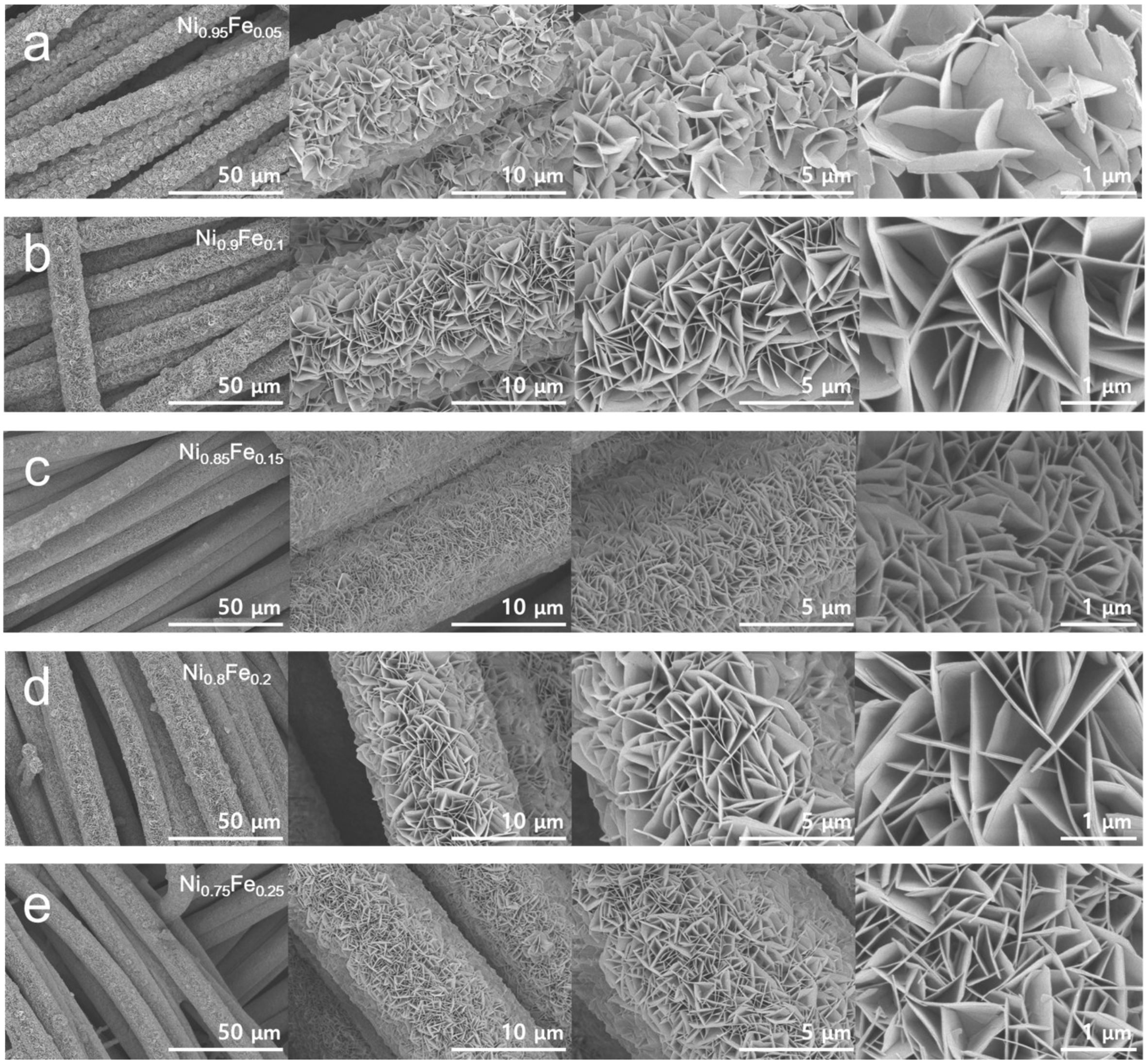

Figure S4. SEM images of NF-LDHs with different Ni:Fe molar ratios.

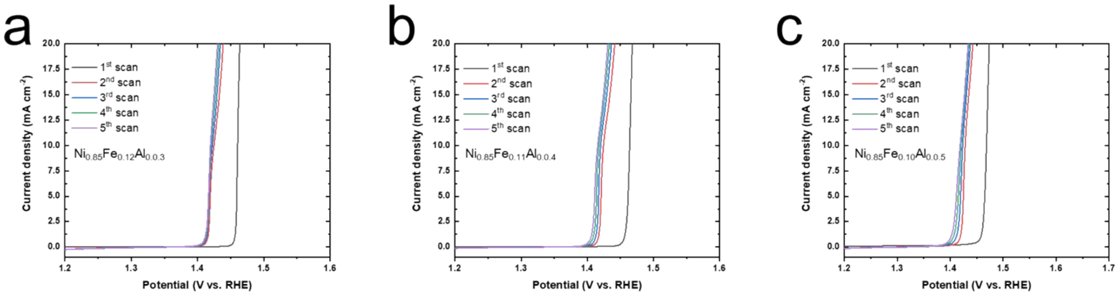

Figure S5. LSV curves for NFA-LDHs with different amounts of Al precursor measured in 1.0 M KOH.

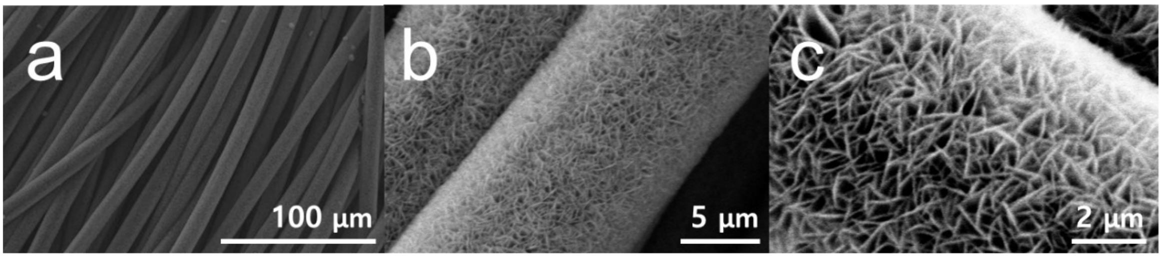

Figure S6. SEM images of NFA-LDHs with the molar ratio of Ni:Fe:Al as 0.95:0.10:0.05.

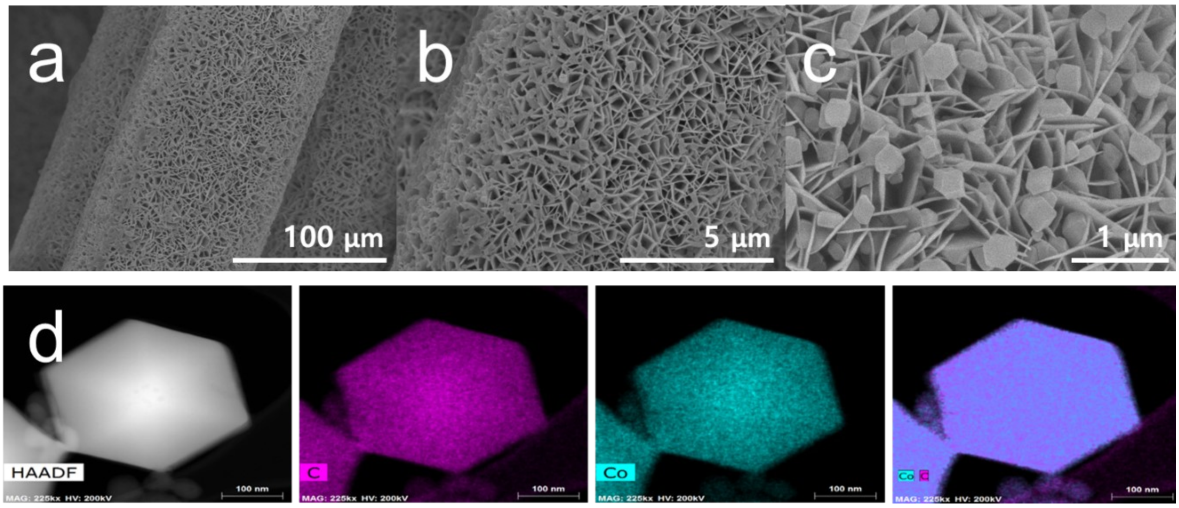

Figure S7. (a-c) SEM images of NFAC-LDHs and (d) the EDX mapping images for the ZIF-67 polyhedrons.

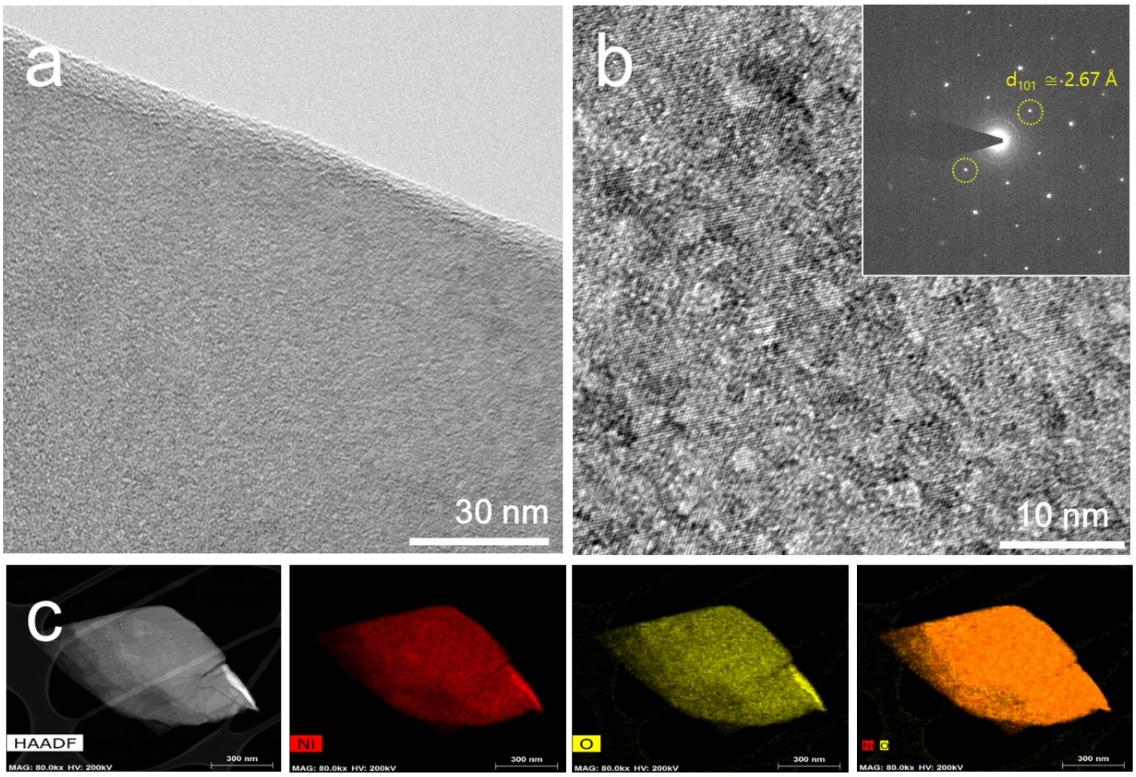

Figure S8. (a-b) HR-TEM images of Ni-LDHs where the inset shows corresponding SAED pattern. (c) EDX mapping images for Ni, O, and overlay.

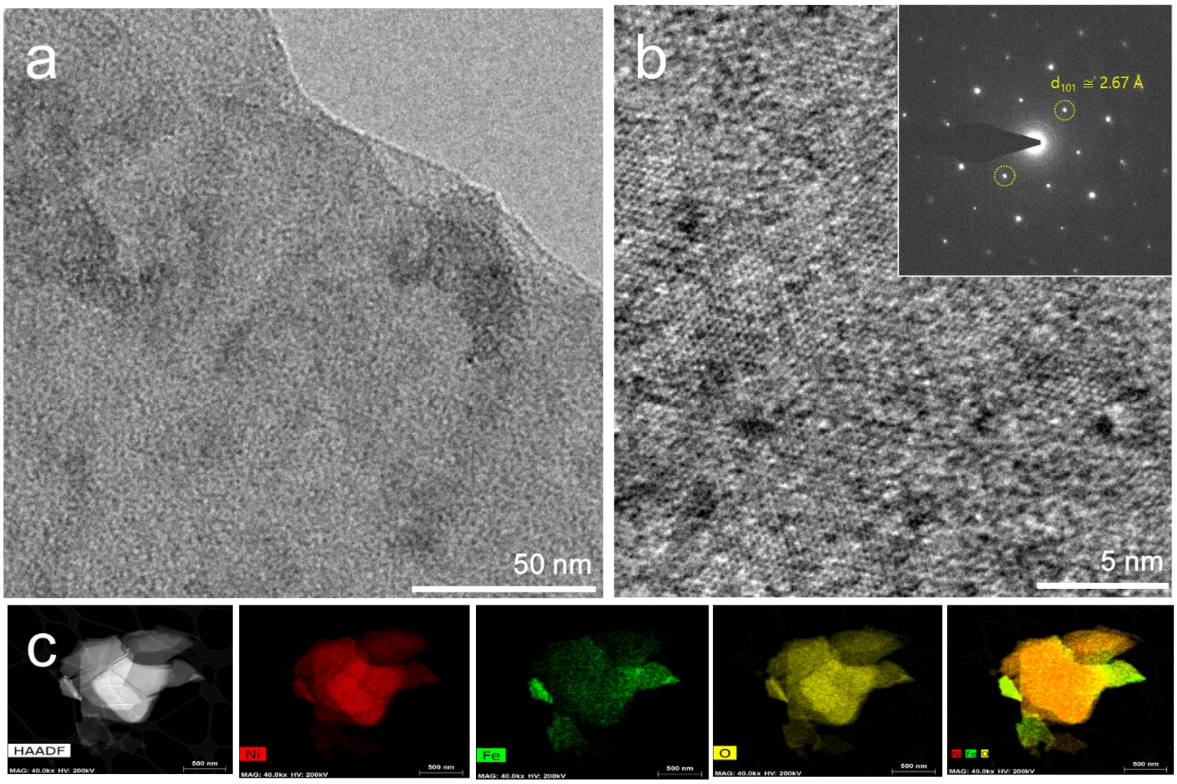

Figure S9. (a-b) HR-TEM images of NF-LDHs where the inset shows corresponding SAED pattern. (c) EDX mapping images for Ni, Fe, O, and overlay.

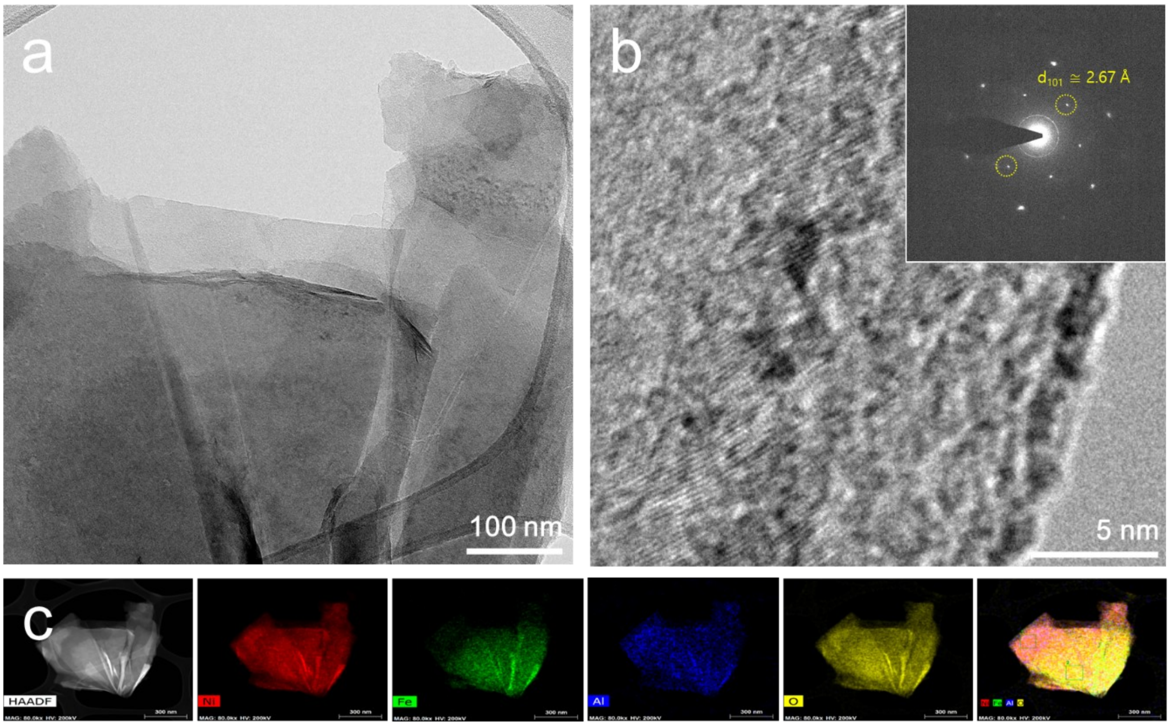

Figure S10. (a-b) HR-TEM images of NFA-LDHs where the inset shows corresponding SAED pattern. (c) EDX mapping images for Ni, Fe, Al, O, and overlay.

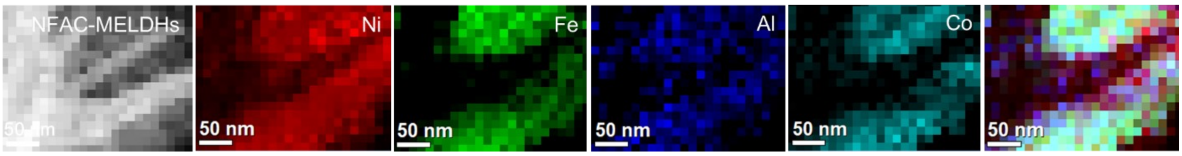

Figure S11. STEM EELS mapping results of NFAC-MELDHs for Ni, Fe, Al, Co, and overlay.

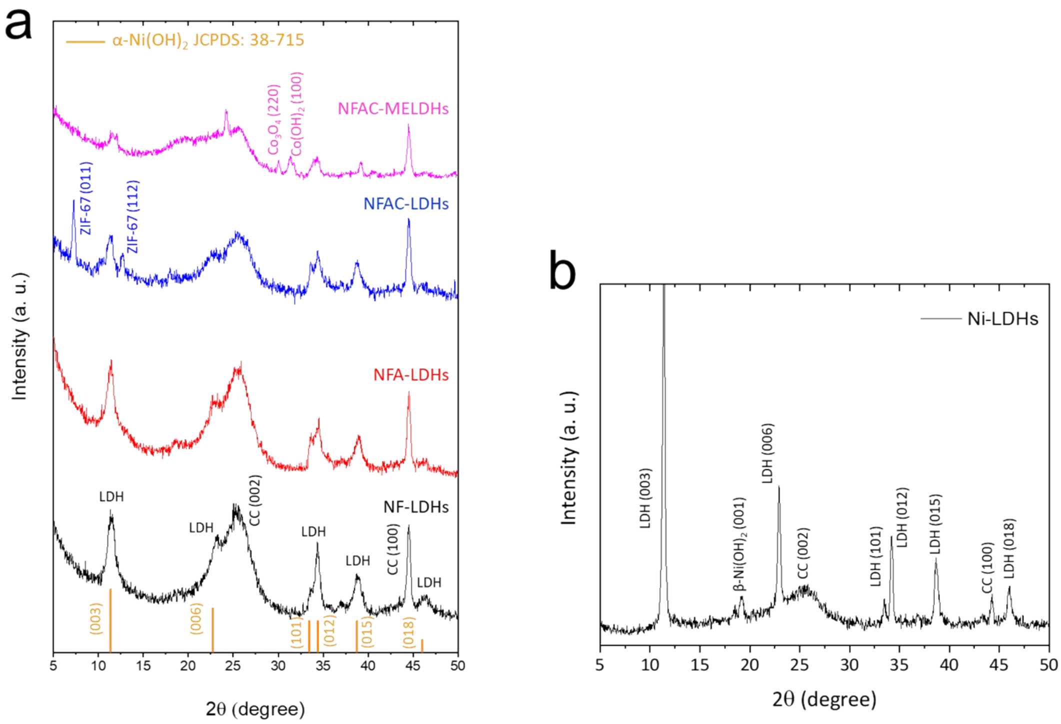

Figure S12. XRD patterns of (a) NF-LDHs, NFA-LDHs, NFAC-LDHs, NFAC-MELDHs and (b) Ni-LDHs.

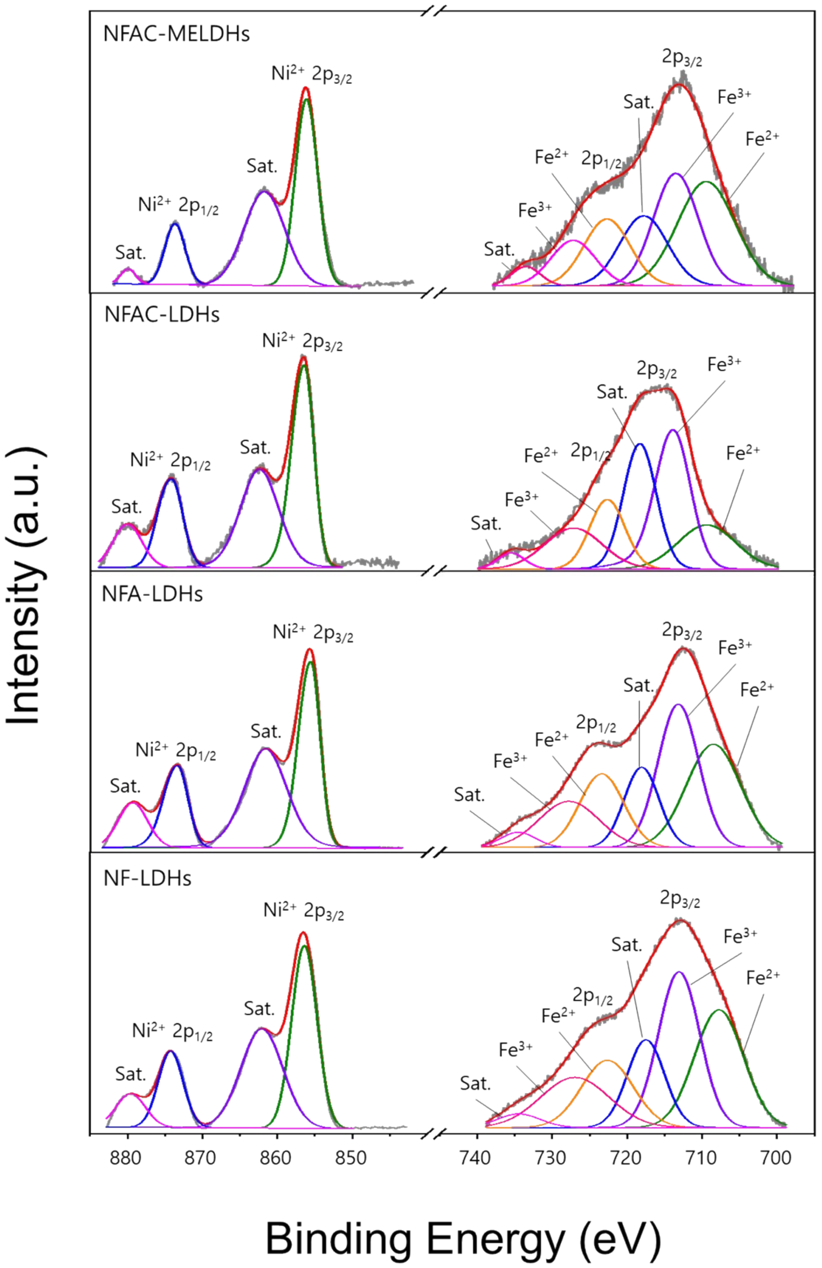

Figure S13. Ni 2p and Fe 2p XPS spectra for NF-LDHs, NFA-LDHs, NFAC-LDHs, and NFAC-MELDHs.

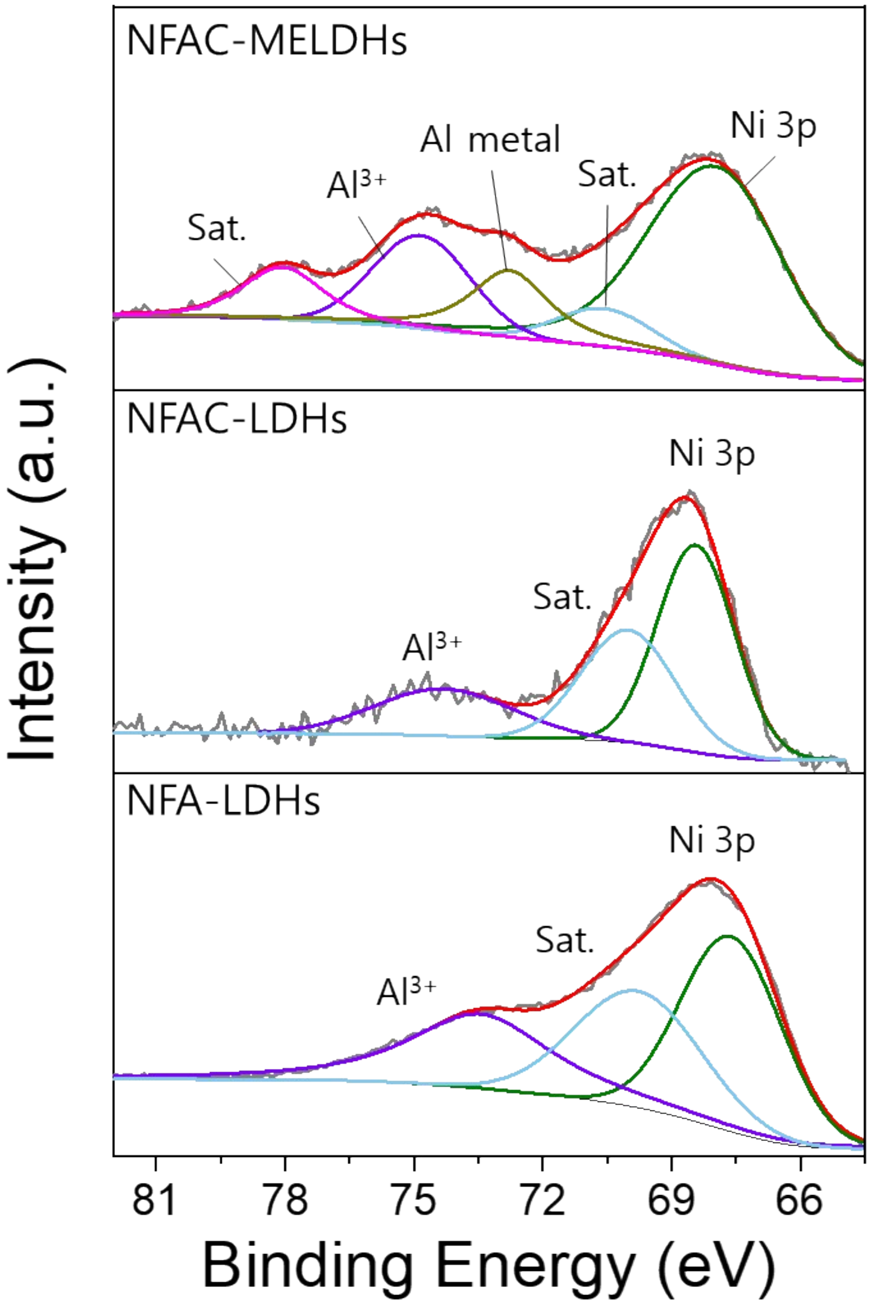

Figure S14. Al 2p XPS spectra for NFA-LDHs, NFAC-LDHs, and NFAC-MELDHs.

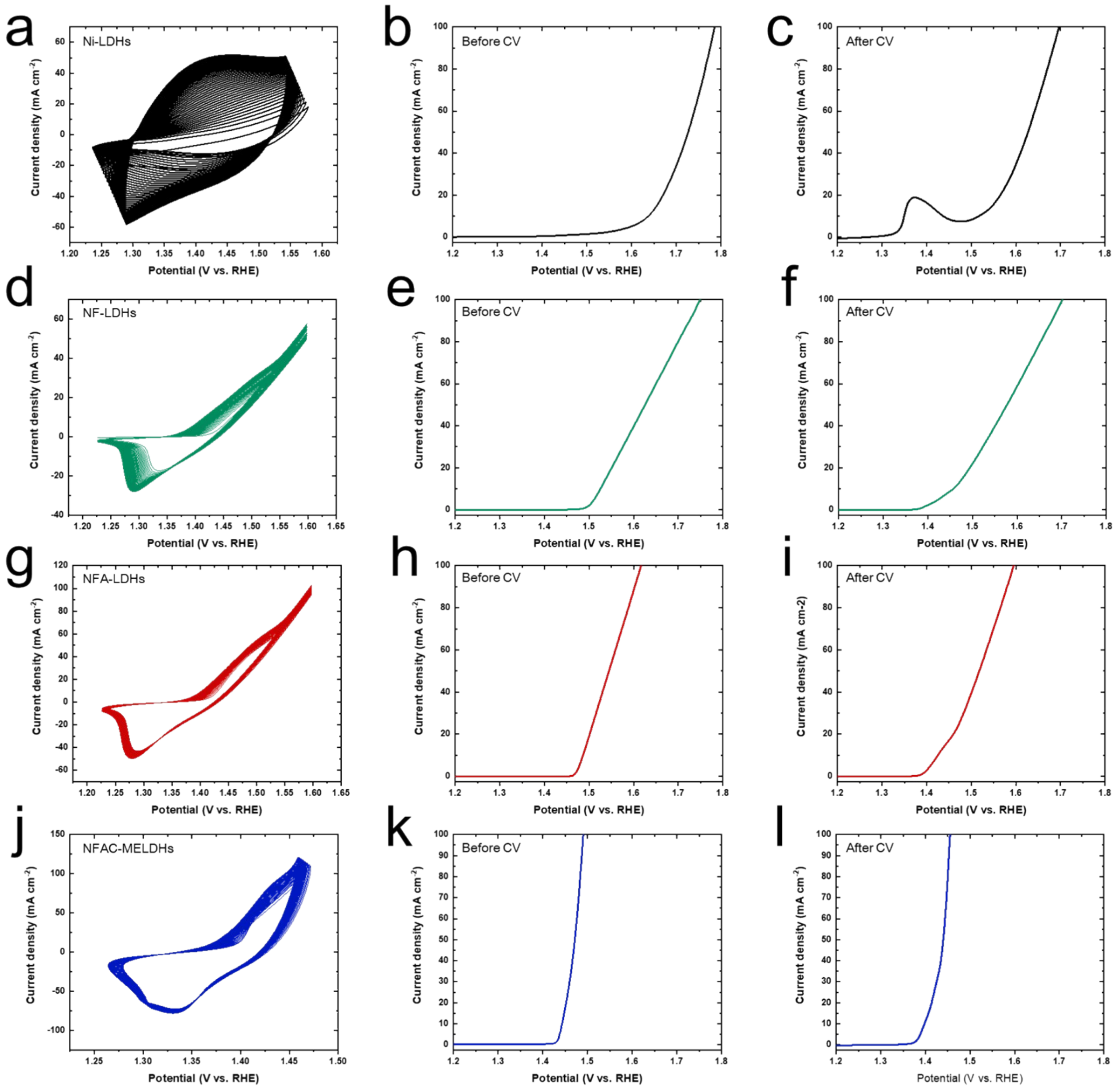

Figure S15. LSV curves before and after CV cycling in 1.0 M KOH for (a-c) Ni-LDHs, (d-f) NF-LDHs, (g-i) NFA-LDHs, and (j-l) NFAC-MELDHs.

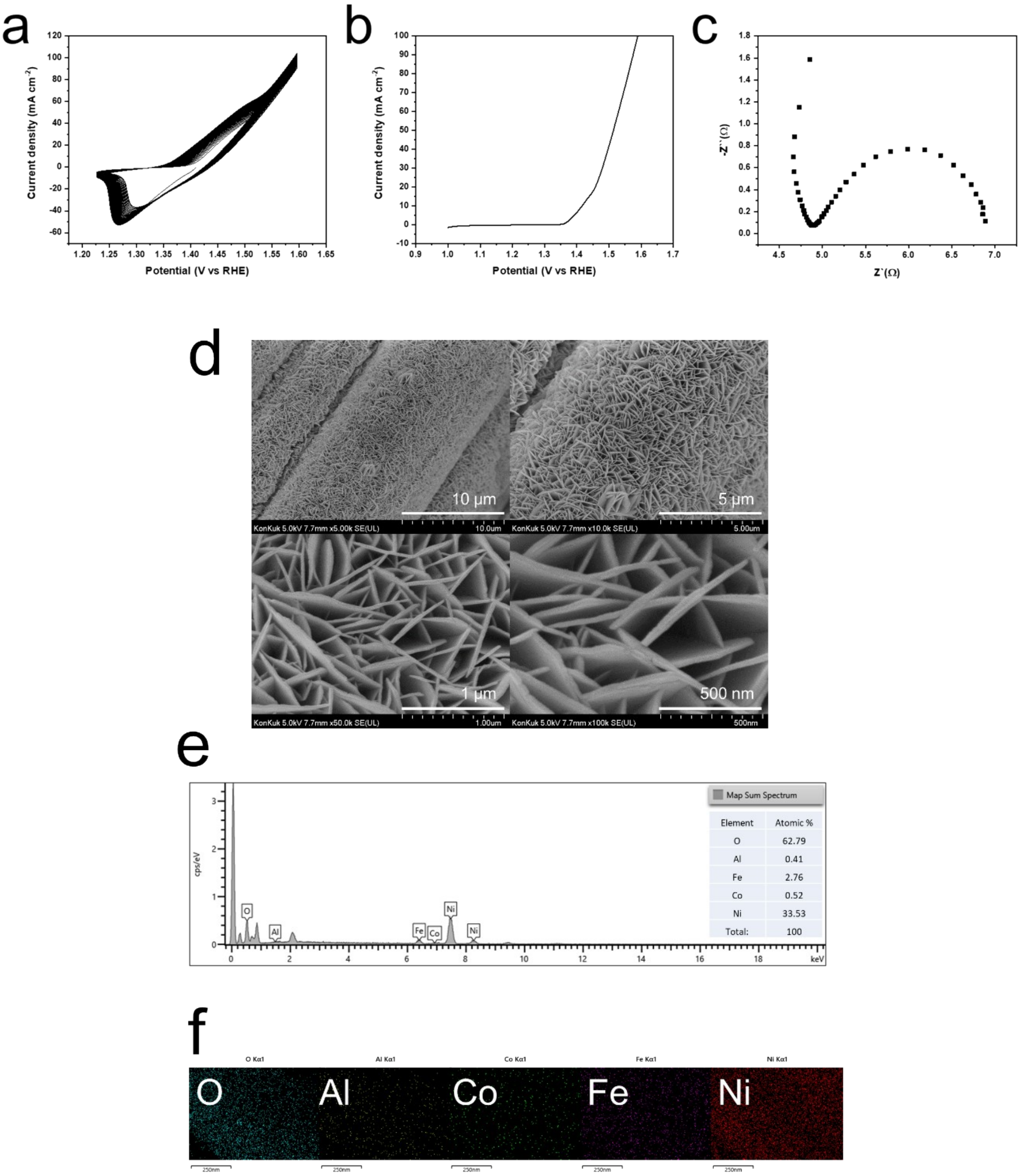

Element	Atomic %
O	62.79
Al	0.41
Fe	2.76
Co	0.52
Ni	33.53
Total:	100

Figure S16. (a) CV cycling, (b) LSV curves, (c) EIS results measured in 1.0 KOH for NFAC-LDHs prepared via one-step hydrothermal reaction. (d) SEM images, (e) EDS spectra, and (f) EDS mapping images for O, Al, Co, Fe, and Ni of the NFAC-LDHs prepared via one-step synthesis.

The SEM and EDS results confirm that of the NFAC-LDHs prepared via one-step synthesis have a morphology and chemical composition comparable to those of the NFAC-MELDHs.

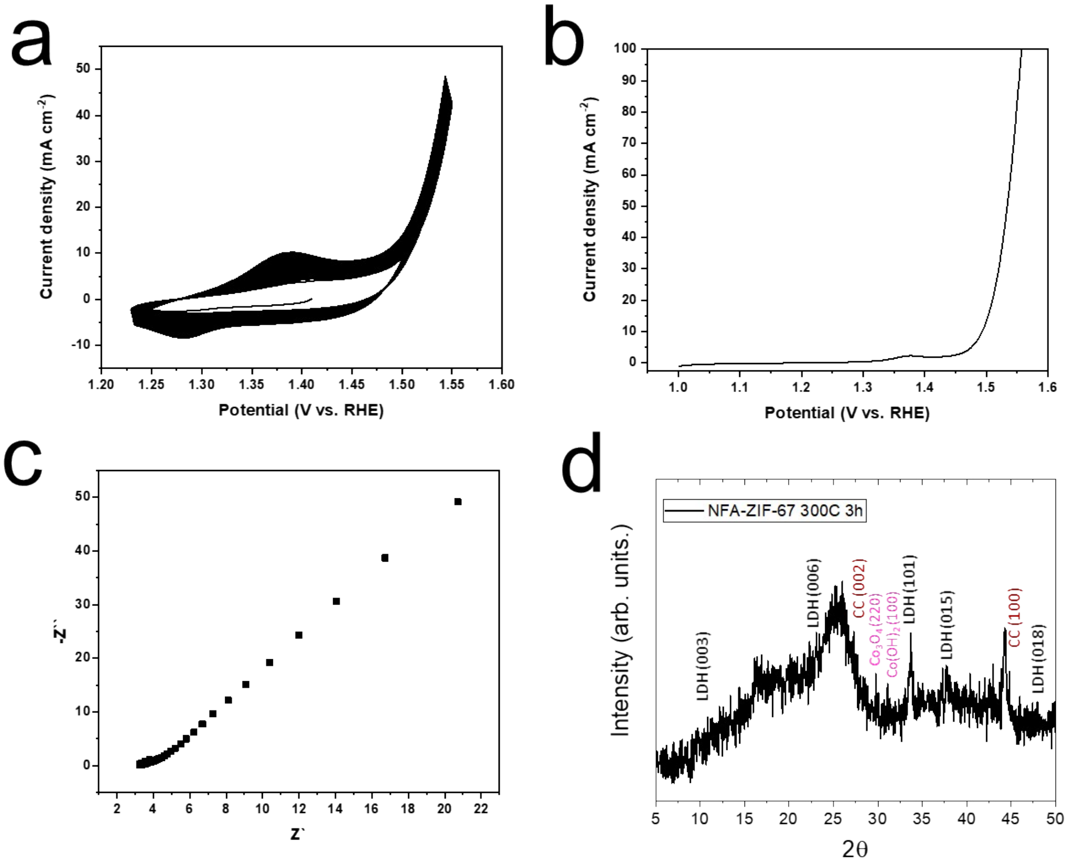

Figure S17. (a) CV cycling, (b) LSV curves, (c) EIS results measured in 1.0 KOH for NFAC-LDHs after a heat treatment at 300°C in an Ar atmosphere for 3 h. (d) XRD pattern of the sample.

The heat treatment at 300 °C for 3 h in an Ar atmosphere induced the conversion of ZIF-67 to the LDH phase with secondary phases of Co oxide and hydroxide which is comparable to the NFAC-MELDHs.

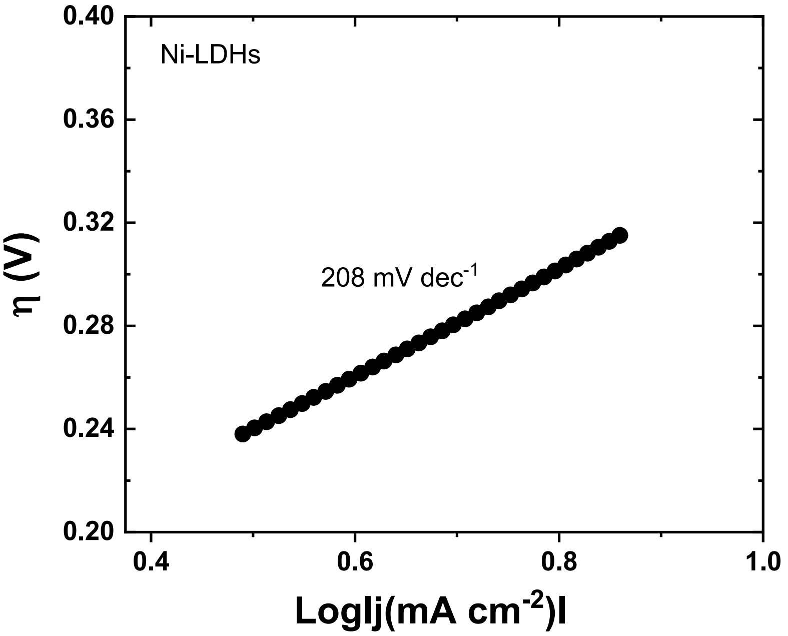

Figure S18. Tafel plot of Ni-LDHs calculated from the LSV curve.

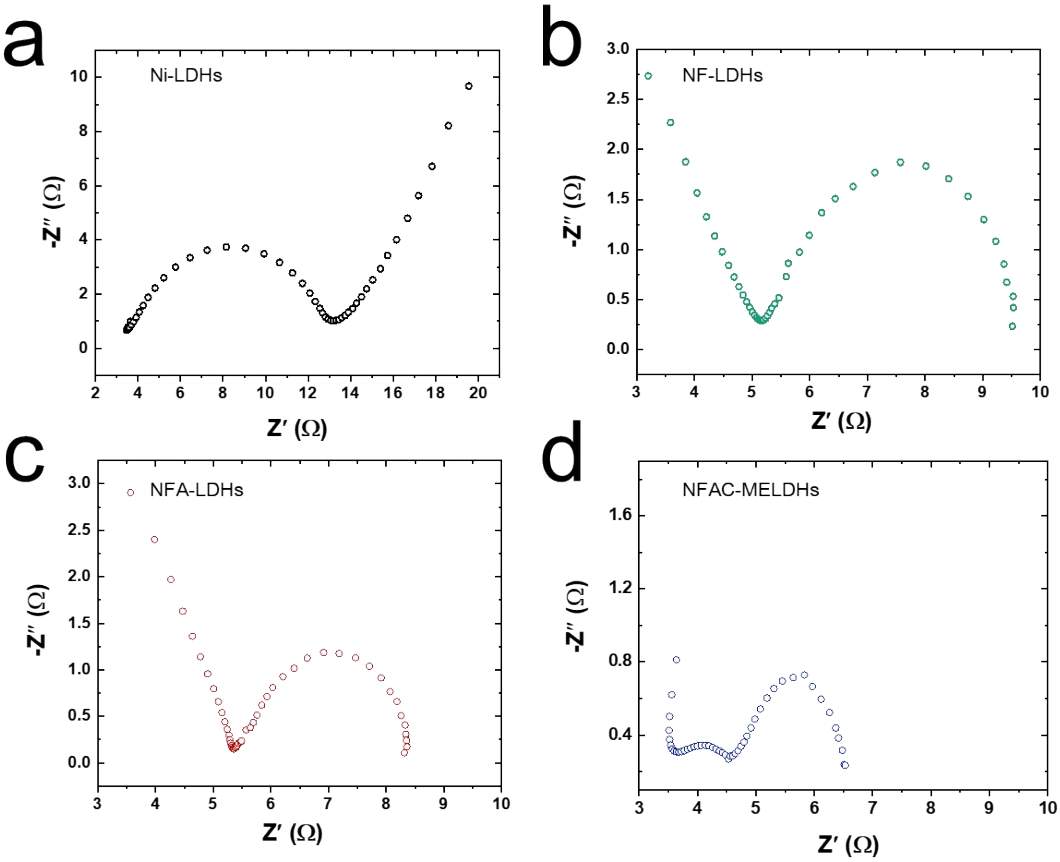

Figure S19. EIS results measured in the frequency range of 0.1–100 kHz at 1.50 V_{RHE} with a sinusoidal amplitude of 5 mV for (a) Ni-LDHs, (b) NF-LDHs, (c) NFA-LDHs, and (d) NFAC-MELDHs.

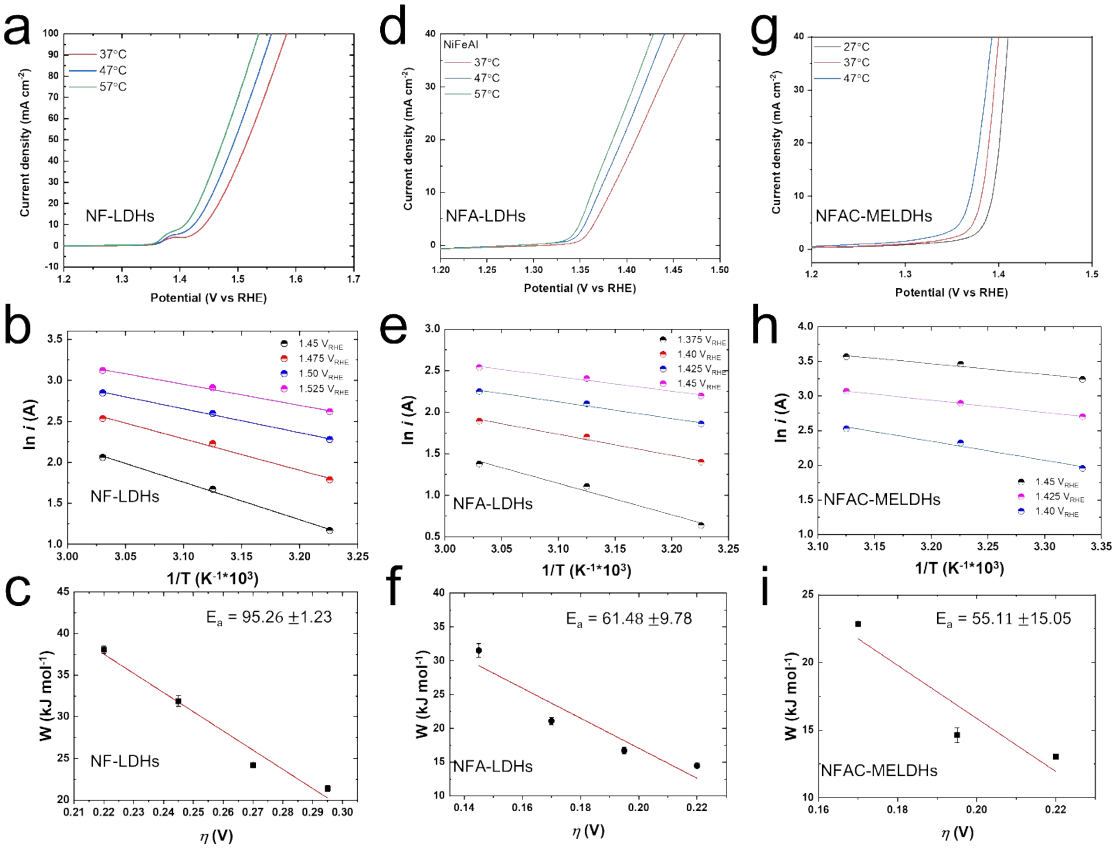

Figure S20. OER LSV curves measured at different electrolyte temperature, Arrhenius plots (ln*i* (A) vs (1/T (K^{-1})), plot of the overall activation energy, W (kJ mol^{-1}), against the reaction overpotential for (a-c) NF-LDHs, (d-f) NFA-LDHs, and (g-i) NFAC-MELDHs.

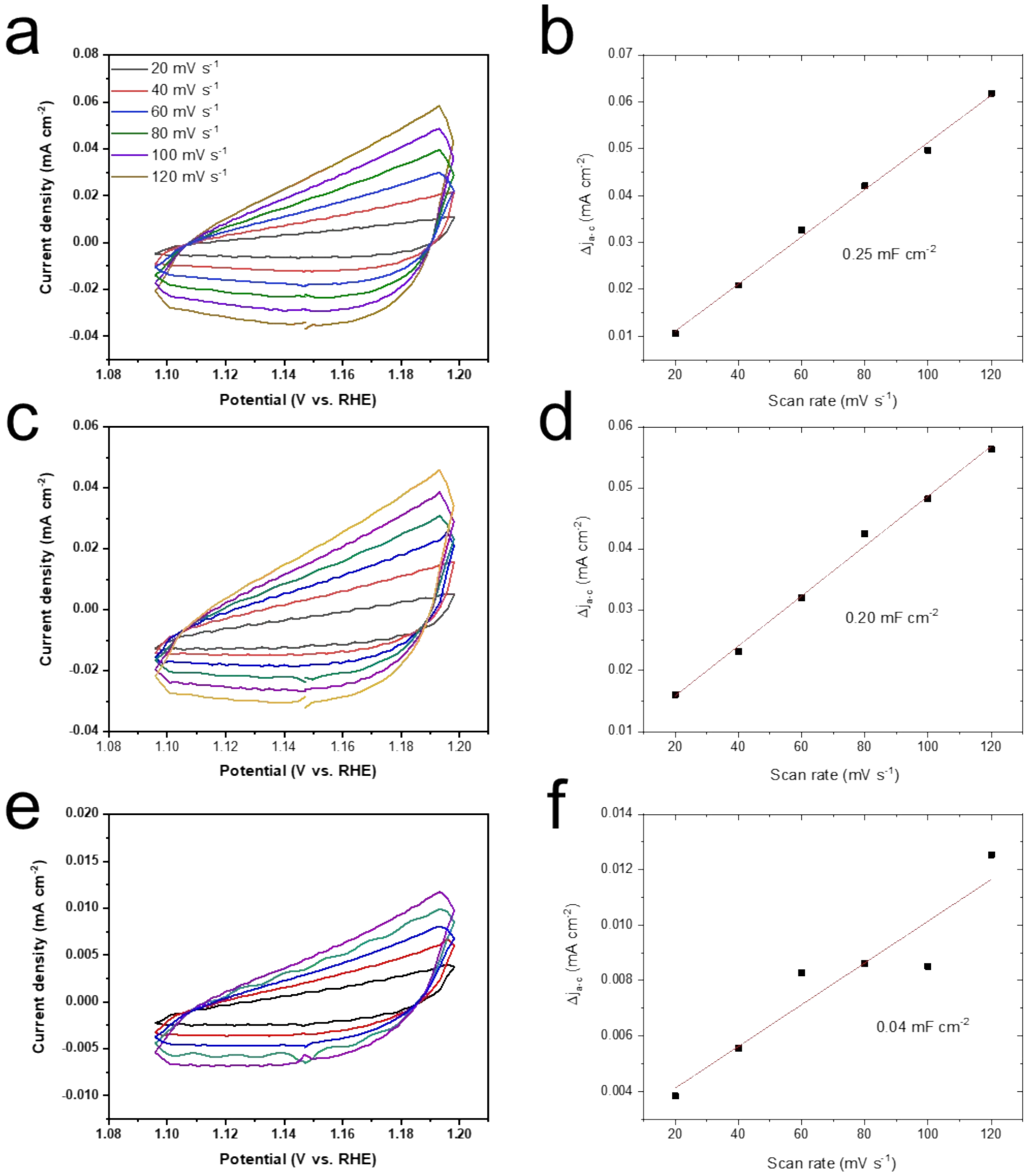

Figure S21. CVs in a capacitive current region (no *iR*-compensated) at scan rates 20, 40, 60, 80, 100, and 120 s^{-1} and the linear plots of Δj_{a-c} vs. scan rates of (a-b) NFAC-MELDHs, (c-d) NFA-LDHs, (e-f) NF-LDHs.

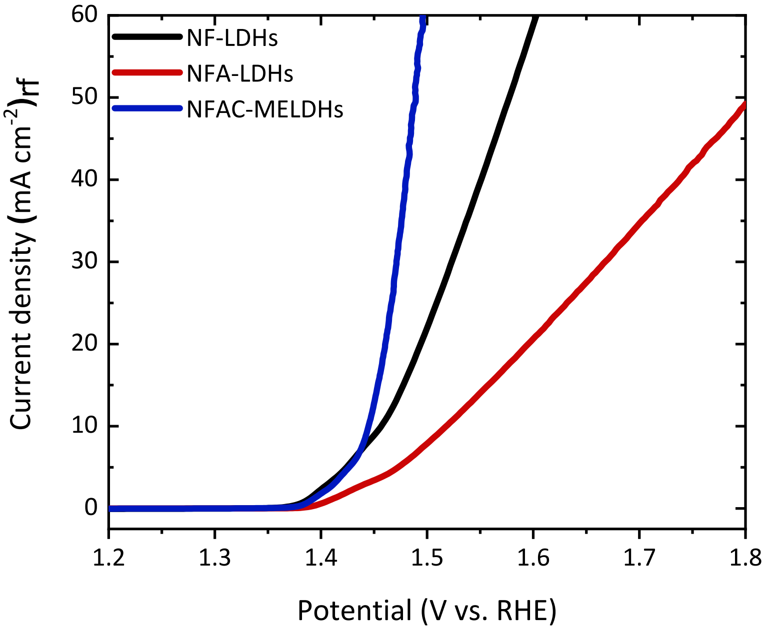

Figure S22. OER LSV curves normalized by rf values for NF-LDHs, NFA-LDHs, and NFAC-MELDHs.

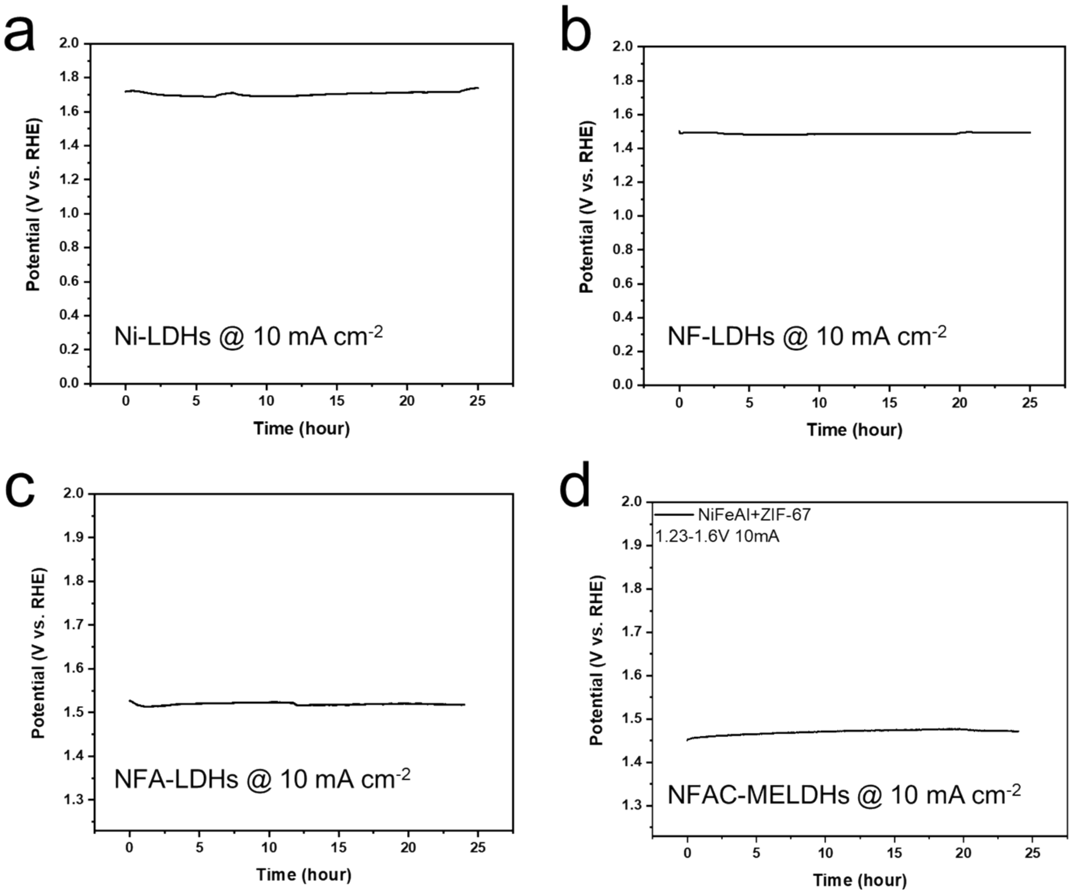

Figure S23. Chronopotentiometry test of (a) Ni-LDHs, (b) NF-LDHs, (c) NFA-LDHs, and (d) NFAC-MELDHs at a constant current density of 10 mA cm^{-2}, in 1.0 M KOH solution.

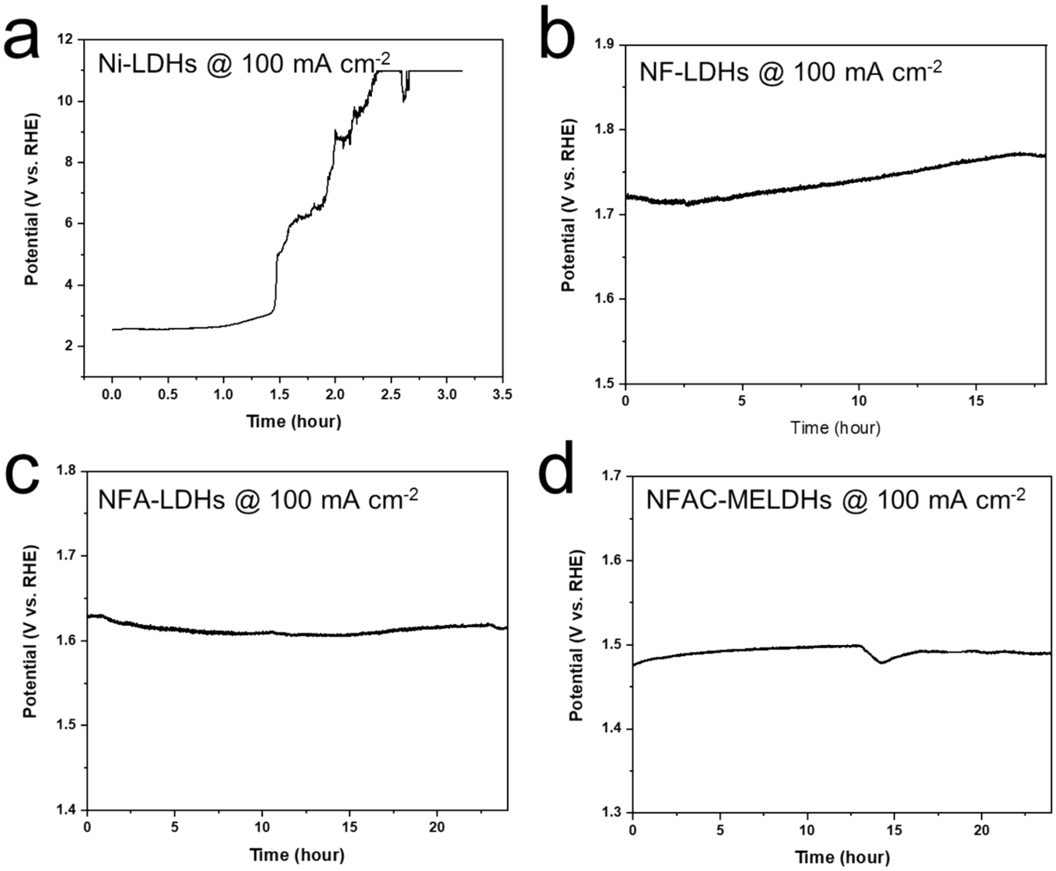

Figure S24. Chronopotentiometry test of (a) Ni-LDHs, (b) NF-LDHs, (c) NFA-LDHs, and (d) NFAC-MELDHs at a constant current density of 100 mA cm^{-2}, in 1.0 M KOH solution.

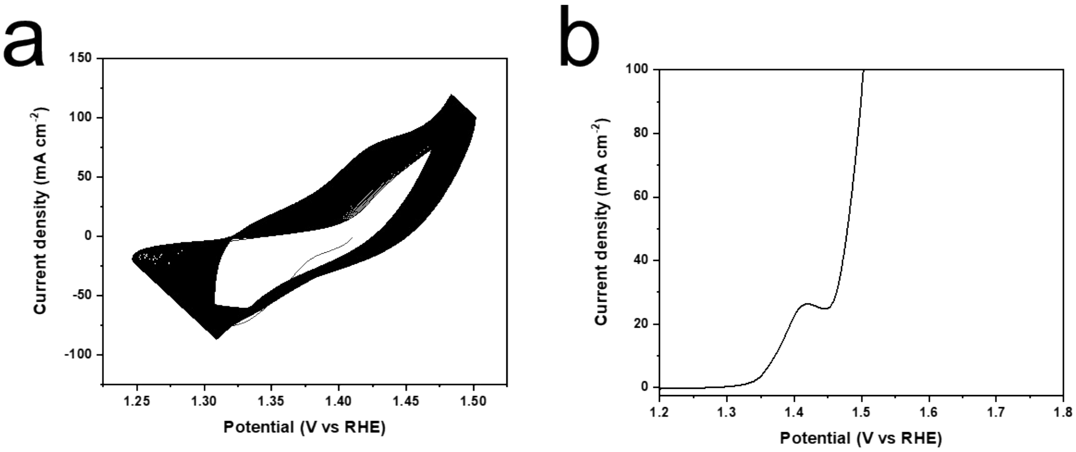

Figure S25. (a) 1000 CV cycling test for NFAC-MELDHs in 1.0 M KOH between 1.25 and 1.50 V_{RHE} with a scan rate of 50 mV s^{-1}. (b) LSV curve of NFAC-MELDHs measured after CV test.

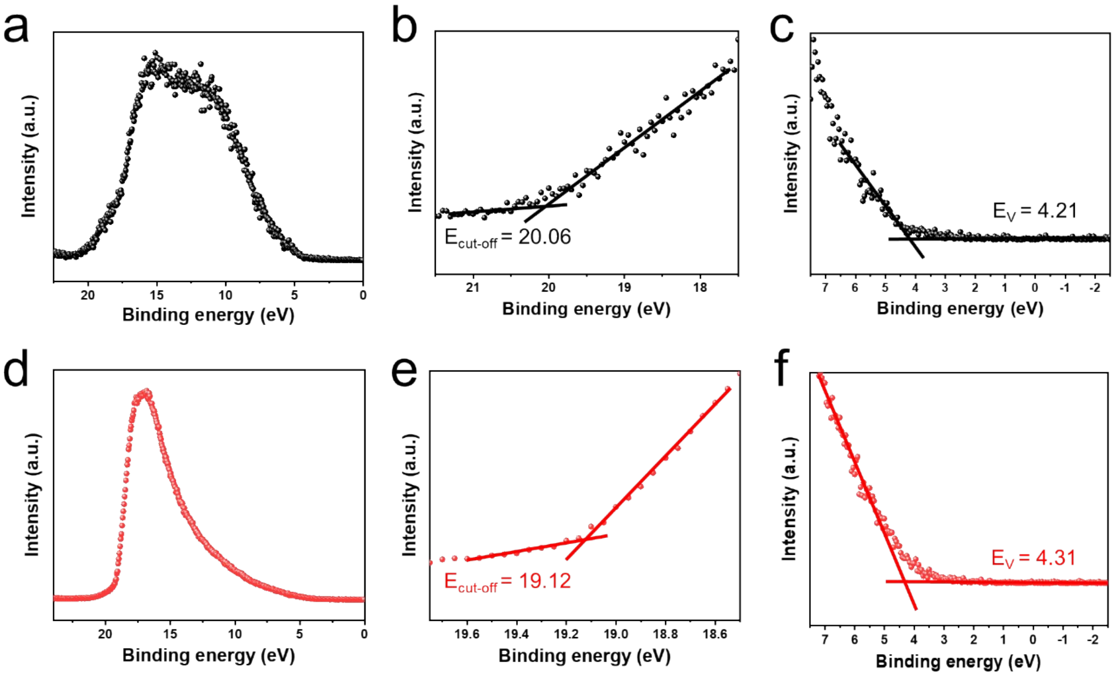

Figure S26. UPS spectra and enlarged UPS spectra for calculating work functions for (a-c) NFA-LDHs and (d-f) NFAC-MELDHs before OER.

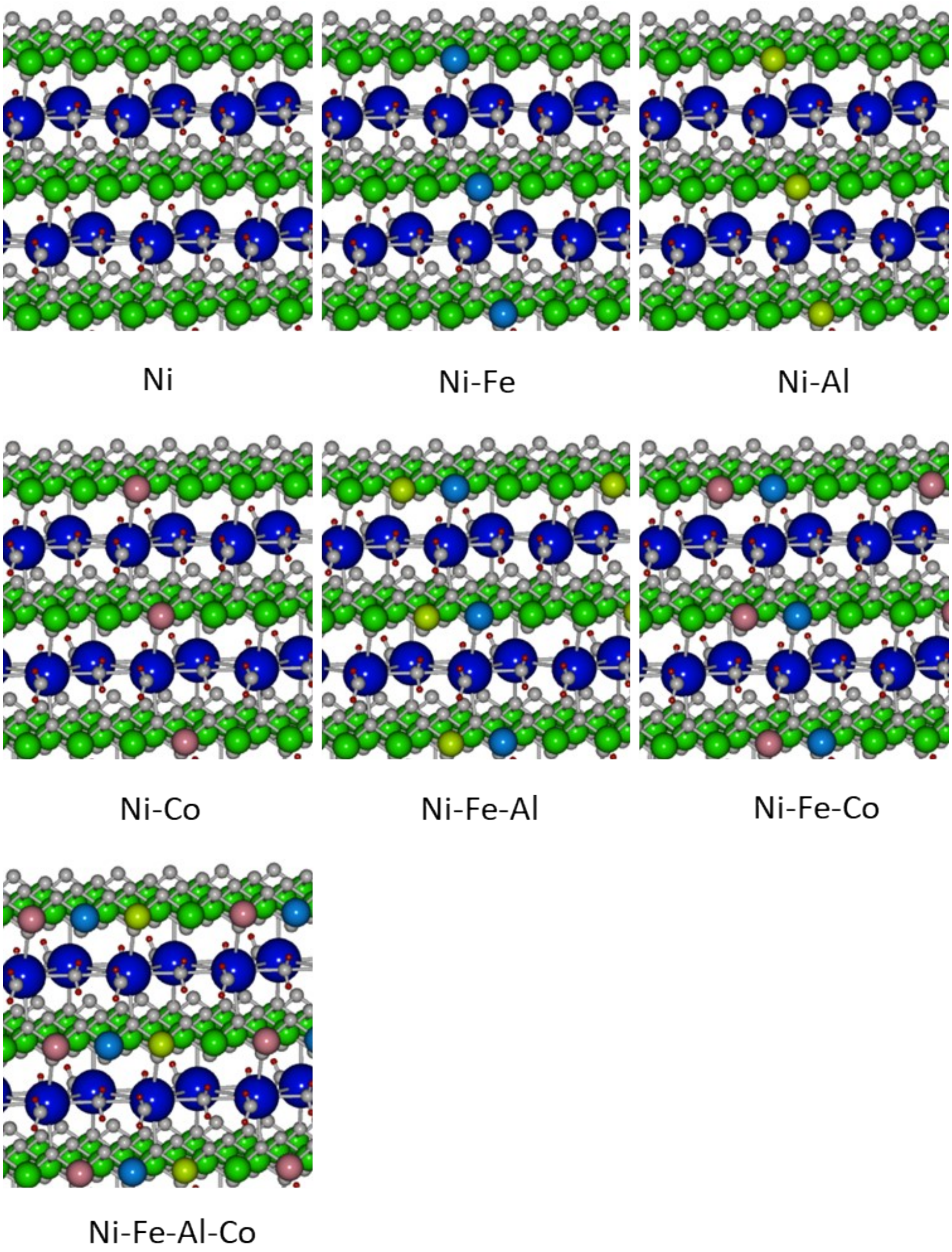

Figure S27. Computed models for unary, binary, ternary, and quaternary Ni-Fe-Al-Co LDHs systems.

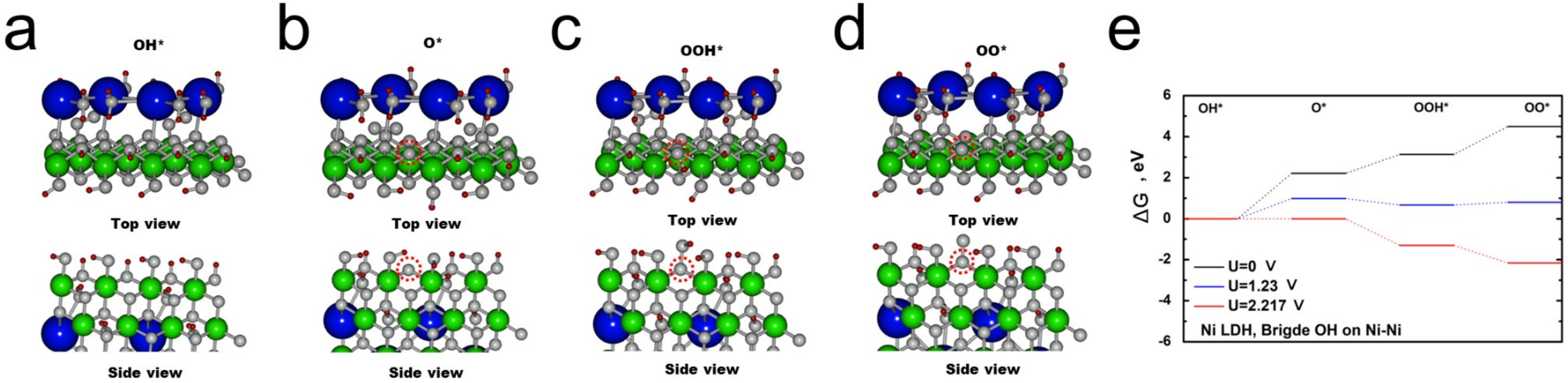

Figure S28. (a-d) OER process on the Ni-Ni bridge site of Ni-LDHs, color – Ni(green), K(blue), O(gray), H(red), and (e) the corresponding calculated free energy diagram for OER process of Ni-LDHs.

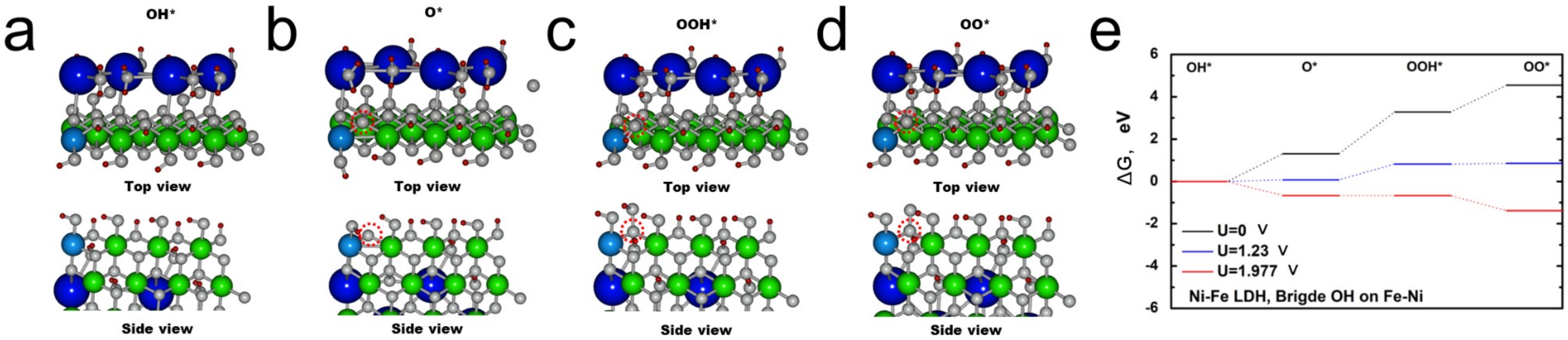

Figure S29. (a-d) OER process on the Ni-Fe bridge site of NF-LDHs, color – Ni(green), Fe(sky blue), K(blue), O(gray), H(red), and (e) the corresponding calculated free energy diagram for OER process of NF-LDHs.

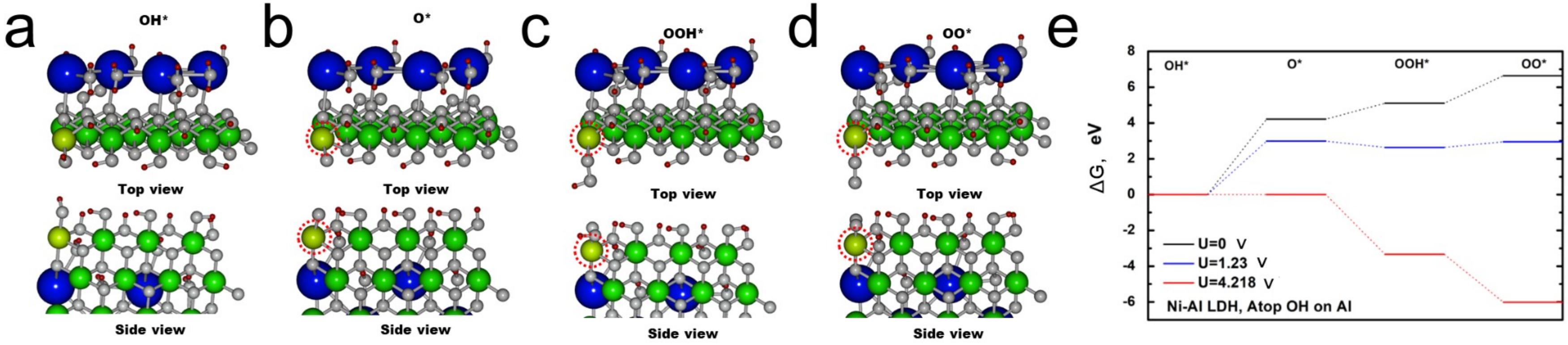

Figure S30. (a-d) OER process on the atop Al site of NA-LDHs, color – Ni(green), Al(yellow), K(blue), O(gray), H(red), and (e) the corresponding calculated free energy diagram for OER process of NA-LDHs.

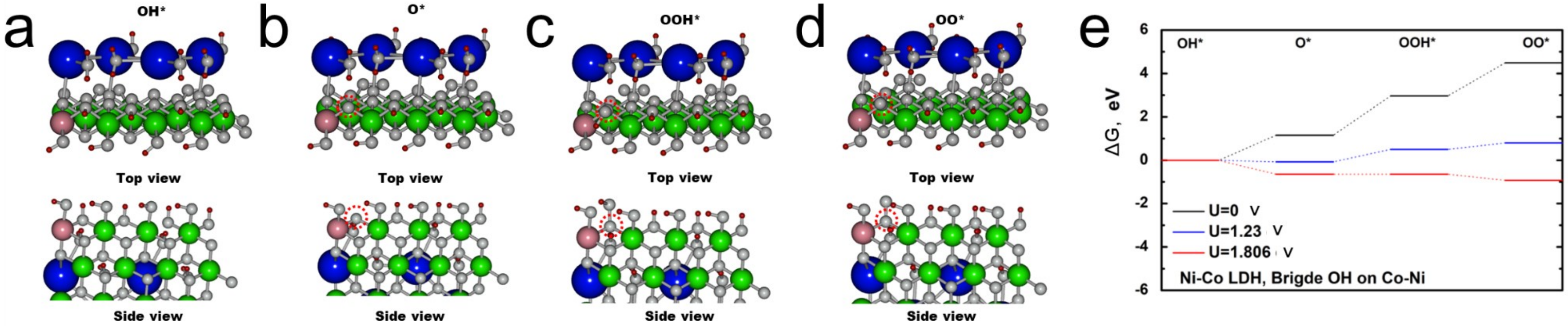

Figure S31. (a-d) OER process on the Ni-Co bridge site of NC-LDHs, color – Ni(green), Co(pink), K(blue), O(gray), H(red), and (e) the corresponding calculated free energy diagram for OER process of NC-LDHs.

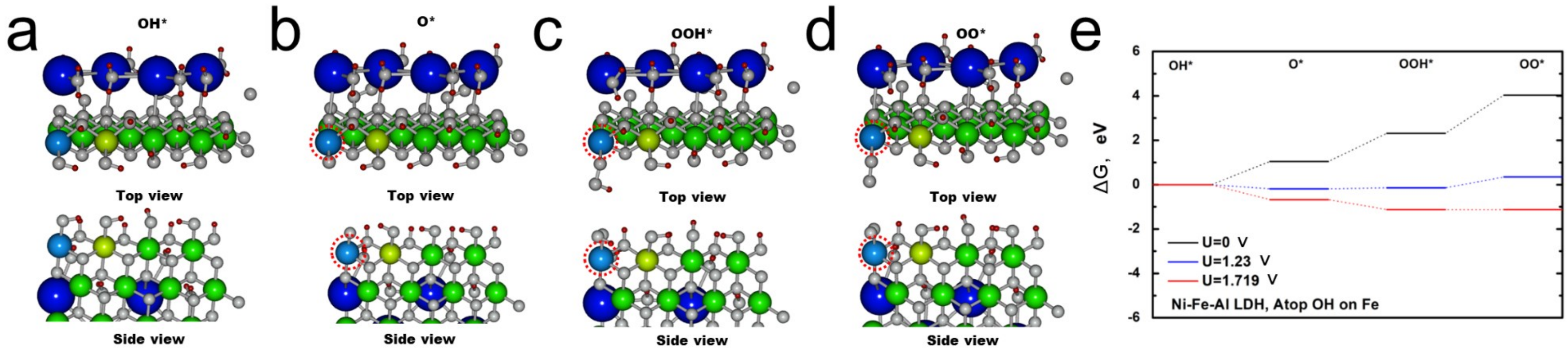

Figure S32. (a-d) OER process on the atop Fe site of NFA-LDHs, color – Ni(green), Fe(sky blue), Al(yellow), K(blue), O(gray), H(red), and (e) the corresponding calculated free energy diagram for OER process of NFA-LDHs.

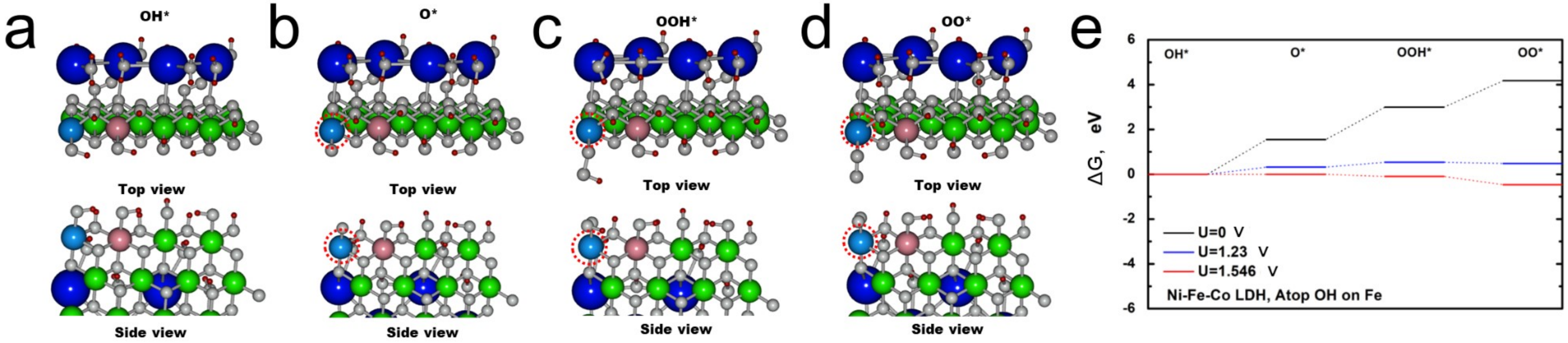

Figure S33. (a-d) OER process on the atop Fe site of NFC-LDHs, color – Ni(green), Fe(sky blue), Co(pink), K(blue), O(gray), H(red), and (e) the corresponding calculated free energy diagram for OER process of NFC-LDHs.

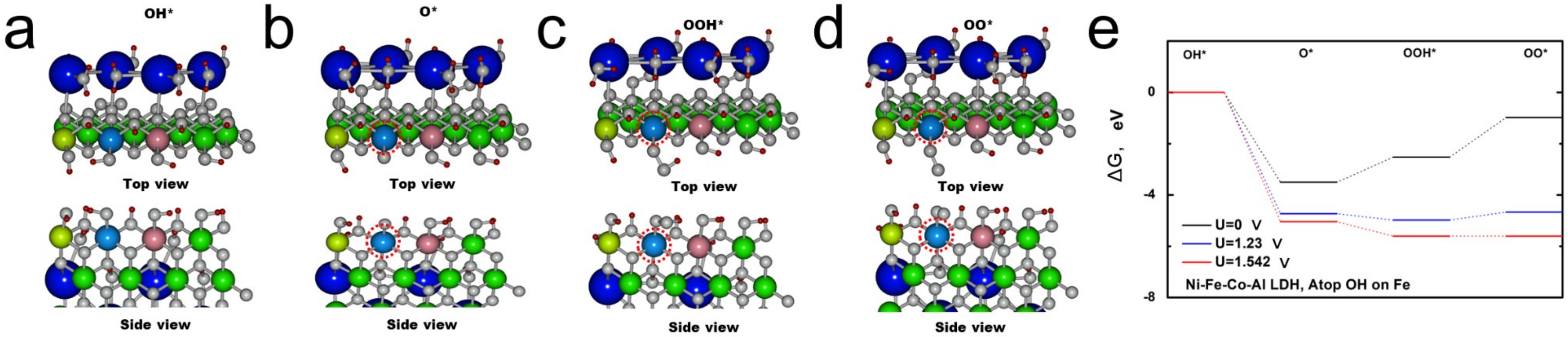

Figure S34. (a-d) OER process on the atop Fe site of NFAC-MELDHs, color – Ni(green), Fe(sky blue), Al(yellow), Co(pink), K(blue), O(gray), H(red), and (e) the corresponding calculated free energy diagram for OER process of NFAC-MELDHs.

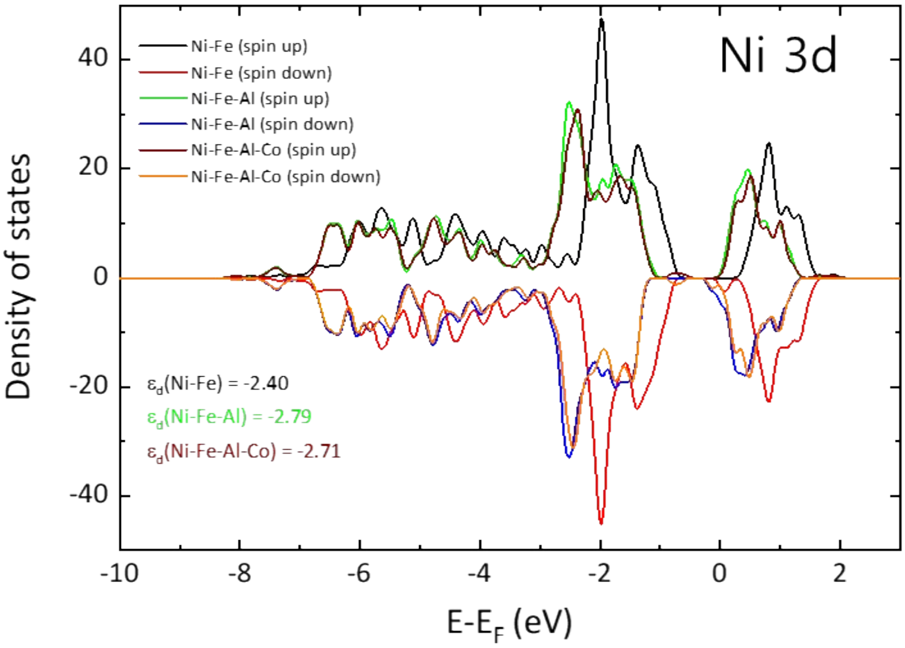

Figure S35. Local density of states of Ni 3d calculated for Ni-Fe-Al-Co LDHs systems.

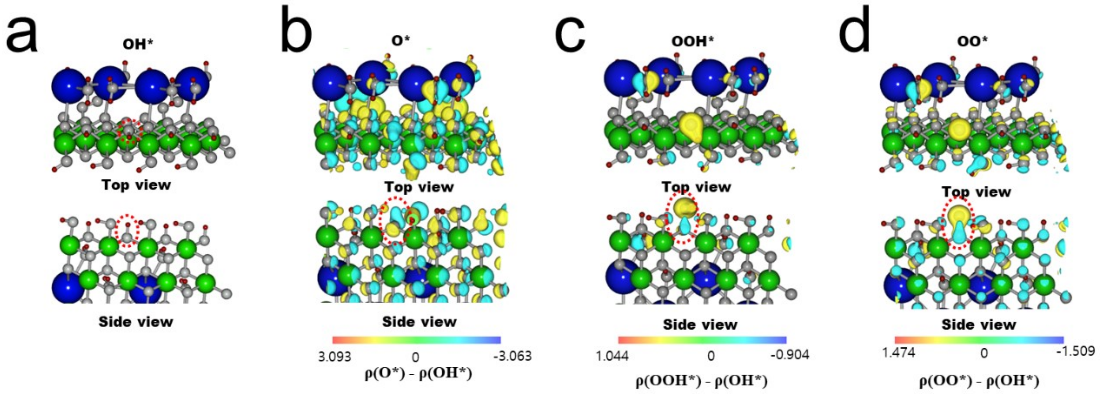

Figure S36. Top and side views for local charge density distributions on the Ni-LDHs for the adsorptions of oxygen intermediates.

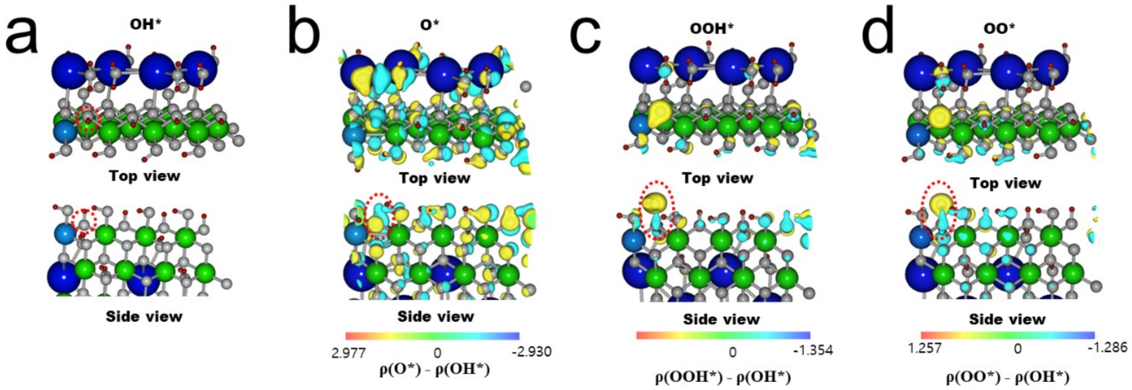

Figure S37. Top and side views for local charge density distributions on the NF-LDHs for the adsorptions of oxygen intermediates.

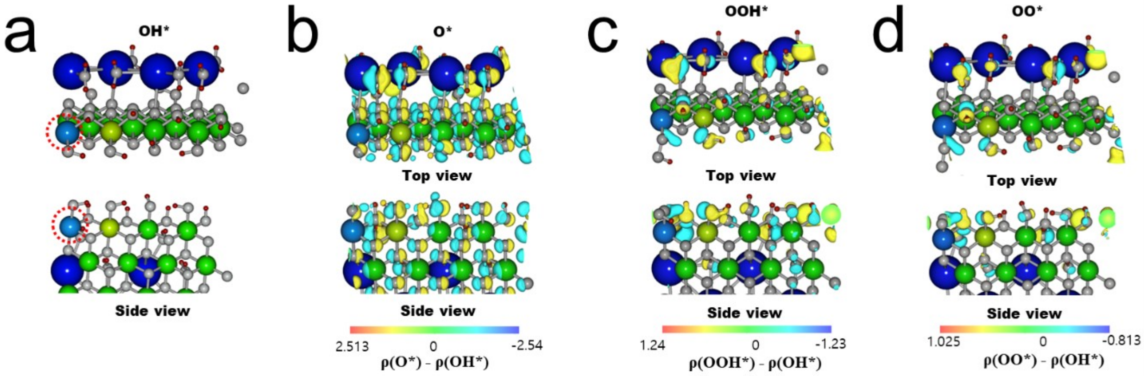

Figure S38. Top and side views for local charge density distributions on the NFA-LDHs for the adsorptions of oxygen intermediates.

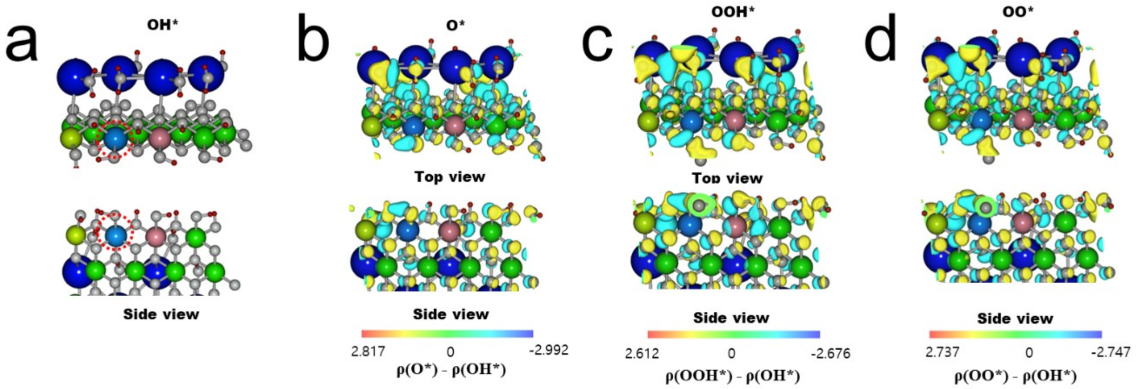

Figure S39. Top and side views for local charge density distributions on the NFAC-MELDHs for the adsorptions of oxygen intermediates.

Table S2. Relative atomic percent in the Ni-Fe-Al-Co LDHs calculated from the quantative EDX and EELS results.

	Ni	Fe	Al	Co	O
Ni-LDHs	36.66	-	-	-	63.34
NF-LDHs	27.30	5.93	-	-	66.78
NFA-LDHs	29.31	5.32	0.91	-	64.45
NFAC-LDHs	30.96	5.94	0.60	0.61	61.90
NFAC-MELDHs (EELS)	26.35	4.35	0.60	1.23	67.47

Table S3. A comparison of catalytic OER activity for NFAC-MELDHs with transition metal based electrocatalysts in alkaline electrolyte.

Catalyst	**Electrolyte**	***η^{10} (mV)**	****η^{100} (mV)**	**Tafel slope (mV dec^{-1})**	**Loading amount (mg cm^{-2})**	**Reference**
NFAC-MELDHs	1 M KOH	160	220	29	0.28	This work
Co_2Fe-LDH	1 M KOH	420	-	83	0.20	S7
ZnCo-LDH	1 M KOH	340	-	-	0.28	S8
CoMn-LDH	1 M KOH	350	-	43	0.22	S9
NiFe-LDH/CNT	1 M KOH	300	340	38		S10
Ni-Fe LDH-0.20M	1 M KOH	243	-	50	0.178	S11
pc-NiFe-LDH/NF	1 M KOH	-	153	30	-	S12
NiFeCr LDH/GC	1 M KOH	280	-	131	-	S13
B-Co_2Fe LDH/NF	1 M KOH	205	246	39.2	-	S14
NiFe LDH	1 M KOH	202	237	32.8	-	S15
Ni-B/NF	1 M KOH	360	-	76	12.3	S16
Co-Ni-B@NF-500	1 M KOH	313	-	120	-	S17
NiCoS/CC NSs	1 M KOH	330	-	109	-	S18
$NiCo_2S_4$ NA/CC	1 M KOH	340	-	89	0.43	S19
NiFeLDH@Au/Ni foam	1 M KOH	-	235	48.4	-	S20
NiCoP/NF	1 M KOH	280	-	87	1.60	S21
NiNO/CC	1 M KOH	-	390	54	0.38	S22
Ru Sas/AC-FeCoNi	1 M KOH	205	-	-	0.25	S23
Ni_2P@NF-6	1 M KOH	-	590	40	3.50	S24
Ni@Co-Ni-P	1 M KOH	-	380	297	3.00	S25

*Overpotential for affording a current density of 10 mA cm^{-2}; **Overpotential for affording a current density of 100 mA cm^{-2}.

Table S4. A **c**omparison of catalytic OER activity for NFAC-MELDHs with transition metal based electrocatalysts in a simulated seawater electrolyte.

Catalyst	**Electrolyte**	**$^*\eta^{10}$ (mV)**	**$^{**}\eta^{100}$ (mV)**	**Loading amount (mg cm^{-2})**	**Reference**
NFAC-MELDHs	1 M KOH + 0.5M NaCl	210	280	0.28	This work
NiMoN@NiFeN	1 M KOH + 0.5M NaCl		286		S26
Co-Fe-O-B*	1 M KOH + 0.5M NaCl	294	434	0.1	S27
CoCH	1 M KOH + 0.5 M NaCl	251	-	-	S28
NiFe-LDH/NFa	1 M KOH + 0.5 M NaCl	-	227	0.32	S29

*Overpotential for affording a current density of 10 mA cm^{-2}; **Overpotential for affording a current density of 100 mA cm^{-2}.

Table S5. Free energy barriers and overpotentials for the formation of O*, OOH* and OO*for all 7 LDH systems.

Absorption energy	Pathway	Ni-LDH	NF-LDH	NA-LDH	NC-LDH	NFA-LDH	NFC-LDH	NFAC-MELDH
ΔG(O*), eV	$OH^* \rightarrow O^*$	2.217	1.308	4.218	1.157	1.044	1.546	-3.502
ΔG(OOH*), eV	$OH^* \rightarrow OOH^*$	3.132	3.286	5.101	2.964	2.318	2.995	-2.521
ΔG(OO*), eV	$OH^* \rightarrow OO^*$	4.495	4.546	6.642	4.487	4.038	4.173	-0.979
η_{OER}, V	-	0.987	0.747	2.988	0.576	0.489	0.316	0.312

Table S6. Bader charge analysis on NFA-LDHs for respective OER steps.

Atomic Index	OH*	O*	OOH*	OO*
1	14.31	14.30	14.34	14.36
2	6.98	6.62	6.34	6.22
3	-	-	6.83	6.06
4	0.37	-	0.00	-

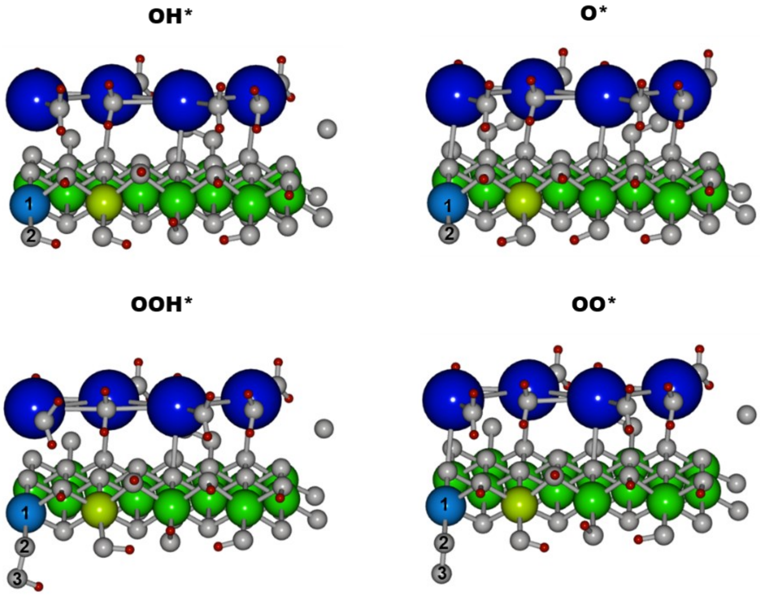

1 = Fe, 2,3 = O, 4=H

Table S7. Bader charge analysis on NFAC-MELDHs for respective OER steps.

Atomic Index	**OH***	**O***	**OOH***	**OO***
1	14.31	14.29	14.34	14.35
2	7.03	6.63	6.39	6.24
3	-	-	6.53	6.13
4	0.38	-	0.32	-

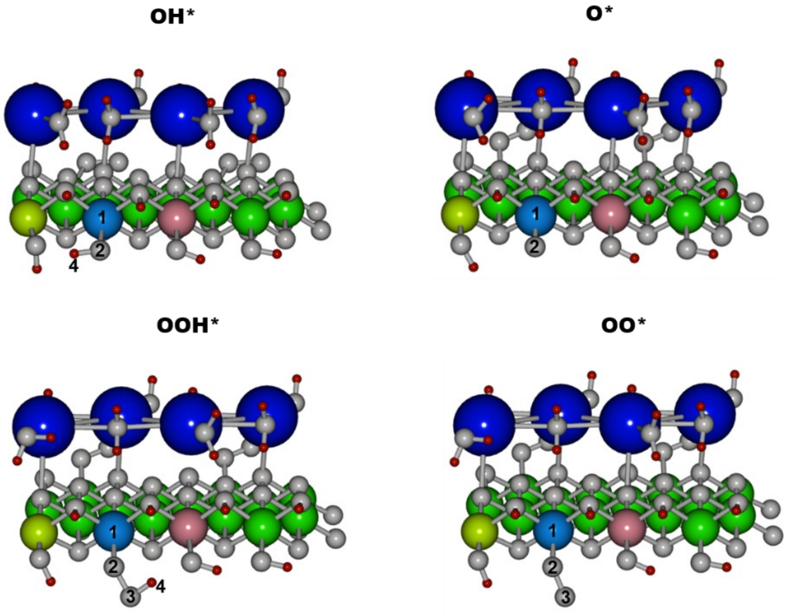

1 = Fe, 2,3 = O, 4=H

Reference for SI

[S1] S. Pintado, S. Goberna-Ferron, E. C. Escudero-Adan, J. R. Galan-Mascaros, J. Am. Chem. Soc., 2013, 135 (36), 13270-13273

[S2] Z. C. Wang, H.L. Liu, R. X. Ge, X. Ren, J. Ren, D. J. Yang, L. X. Zhang, X. P. Sun, ACS Catal., 2018, 8 (3), 2236-2241

[S3] H. F. Liang, A. N. Gandi, D. H. Anjum, X.B. Wang, U. Schwingenschlogl, H. N. Alshareef, Nano Lett., 2016, 16 (12), 7718-7725

[S4] Z. Xue, X. Zhang, J. Qin, R. Liu, J. Mater. Chem. A, 2019, 7, 23091–23097

[S5] X. Bo, R. K. Hocking, S. Zhou, Y. Li, X. Chen, J. Zhuang, Y. Du, C. Zhao, Energy Environ. Sci., 2020, 13, 4225–4237.

[S6] F. Dionigi, Z. Zeng, I. Sinev, T. Merzdorf, S. Deshpande, M. B. Lopez, S. Kunze, I. Zegkinoglou, H. Sarodnik, D. Fan, A. Bergmann, J. Drnec, J. F. Araujo, M. Gliech, D. Teschner, J. Zhu, W. X. Li, J. Greeley, B. R. Cuenya, P. Strasser, Nat. Commun., 2020, 11, 1–10

[S7] L.X. Feng, A. R. Li, Y. X. Li,; J. Liu, L. D. Y. Wang, L. Y. Huang, Y. Wang, X. B. Ge, ChemPlusChem, 2017, 82 (3), 483-488

[S8] X. Zou, A. Goswami, T. Asefa, J. Am. Chem. Soc., 2013, 135 (46), 17242-17245

[S9] F. Song, X. L. Hu, J. Am. Chem. Soc., 2014, 136 (47), 16481-16484

[S10] Y. B. Li, C. Zhao, ACS Catal., 2017, 7 (4), 2535-2541

[S11] C.Wu, H.Li, Z.Xia, X.Zang, R.Deng, S.Wang, G.Sun, ACS Catal.2020, 10 (19), 11127-11135

[S12] Hongying Li, Xueliang Wang, Tao Wang, Fengxia Xiao, J.Alloys.Com, 2020, 844, 156224

[S13] Y.Yang, L.Dang, M.J.Shearer, H.Sheng, W.Li, J.Chen, P.Xiao, Y.Zhang, R.J.Hamers, S.Jin Adv.Ener.Mater, 2018, 8, 1703189

[S14] L.Wu, L.Yu, Q.Zhu, B.McElhenny, F.Zhang, C.Wu, X.Xing, J.Bao, S.Chen, Z.Ren, Nano.Energ., 2021, 83, 105838

[S15] M.Ning, L.Wu, F.Zhang, D.Wang, S.Song, T.Tong, J.Bao, S.Chen, L.Yu, Z.Ren, Materials Toady Physics, 2021, 19, 100419

[S16] Y. Liang, X. Sun, A. Asiri, Y. He, Nanotechnology, 2016, 27, 12LT01

[S17] N. Xu, G. Cao, Z. Chen, Q. Kang, H. Dai, P. Wang, J. Mater. Chem. A, 2017, 5, 12379

[S18] C. Tang, Z. H. Pu, Q. Liu, A. M. Asiri, Y. L. Luo, X. P. Sun, Int. J. Hydrogen Energ., 2015, 40, 4727

[S19] D. N. Liu, Q. Lu, Y. L. Luo, X. P. Sun, A. M. Asiri, Nanoscale, 2015, 7, 15122

[S20] W.Zhu, L.Liu, Z.Yue, W.Zhang, X.Yue, J.Wang, S.Yu, L.Wang, J.Wang, ACS Appl. Mat. Interface, 2017, 14, 19807-19814

[S21] H. Liang, A. N. Gandi, D. H. Anjum, X. Wang, U. Schwingenschlogl, H. N. Alshareef, Nano Lett., 2016, 16, 7718

[S22] J. Huang, Y. Sun, X. Du, Y. Zhang, C. Wu, C. Yan, Y. Yan, G. Zou, W. Wu, R. Lu, Y. Li, J. Xiong, Adv. Mater., 2018, 30, 1803367

[S23] Y.Hu, G.Luo, L.Wang, X.Liu, Y.Qu, Y.Zhou, F.Zhou, Z.Li, Y.Li, T.Yao, C.Xiong, B.Yang, Z.Yu, Y.Wu, Adv. Energ. Mater., 2021, 11, 2002816

[S24] J. Zheng, W. Zhou, T. Liu, S. Liu, C. Wang, L. Guo, Nanoscale, 2017, 9, 4409-4418

[S25] W. Li, X. Gao, X. Wang, D. Xiong, P. Huang, W. Song, X. Bao, L. Liu, Journal of Power Sources, 2016, 330, 156-166.

[S26] L.Yu, Q.Zhu, S.Song, B.McElhenny, D.Wang, C.Wu, Z.Qin, J.Bao, Y.Yu, S.Chen, Z.Ren, Natur.commun., 2019, 10, 5106

[S27] S.Gupta, M.Forster, A.Yadav, A.J.Cowan, N.Patel, M.Patel, ACS AEM 2020, 3, 7619-7628

[S28] G.Li, Y.Zhao, W.Li, Z.Zhao, Y.Li, H.Yang, K.Fan, P.Zhang, L.Sun, ACS Sustainable Chem. Eng. 2021, 9, 905–913

[S29] Q.Tu, W.Liu, M.Jiang, W.Wang, Q.Kang, P.Wang, W.Zhou, F.Zhou ACS Appl. Ener. Mater., 2021, doi.org/10.1021/acsaem.1c00262